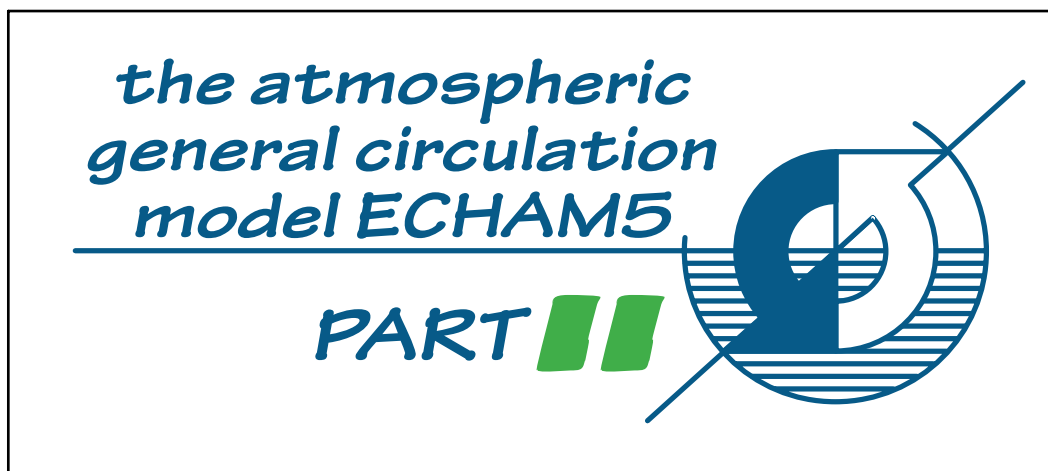




Report No. 354



Sensitivity of Simulated Climate to
Horizontal and Vertical Resolution

by

E. Roeckner • R. Brokopf • M. Esch • M. Giorgetta • S. Hagemann

L. Kornbluh • E. Manzini • U. Schlese • U. Schulzweida

Hamburg, September 2004

Authors

E. Roeckner, R. Brokopf,
M. Esch, M. Giorgetta,
S. Hagemann, L. Kornbluh,
U. Schlese, U. Schulzweida

Max-Planck-Institut für Meteorologie
Hamburg, Germany

E. Manzini

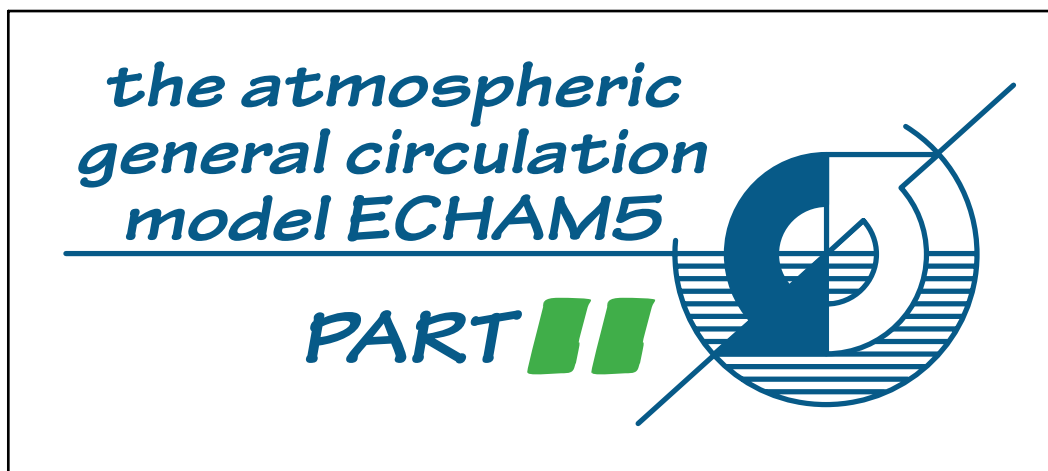
Istituto Nazionale di Geofisica e Vulcanologia,
Bologna, Italy

Max-Planck-Institut für Meteorologie
Bundesstrasse 53
D - 20146 Hamburg
Germany

Tel.: +49-(0)40-4 11 73-0
Fax: +49-(0)40-4 11 73-298
e-mail: <name>@dkrz.de
Web: www.mpimet.mpg.de



Report No. 354



Sensitivity of Simulated Climate to
Horizontal and Vertical Resolution

by

E. Roeckner • R. Brokopf • M. Esch • M. Giorgetta • S. Hagemann

L. Kornblueh • E. Manzini¹ • U. Schlese • U. Schulzweida

Hamburg, September 2004

ISSN 0937 - 1060

¹Istituto Nazionale di Geofisica e Vulcanologia, Bologna, Italy

Abstract

The most recent version of the Max Planck Institute for Meteorology atmospheric general circulation model, ECHAM5, is used to study the impact of changes in horizontal and vertical resolution on seasonal mean climate. In a series of AMIP-style experiments with resolutions ranging between T21L19 and T159L31, the systematic errors and convergence properties are assessed for two vertical resolutions. At low vertical resolution (L19) there is no evidence for convergence to a more realistic climate state for resolutions higher than T42. At higher vertical resolution (L31), on the other hand, the root-mean-squared-errors decrease monotonously with increasing horizontal resolution. Furthermore, except for T42, the L31 versions are superior to their L19 counterparts, and the improvements become more evident at increasingly higher horizontal resolutions. This applies, in particular, to the zonal mean climate state and also to stationary wave patterns in boreal winter. As in previous studies, increasing horizontal resolution leads to a warming of the troposphere, most prominently at mid-latitudes and, hence, to a poleward shift and intensification of the mid-latitude westerlies. Increasing the vertical resolution has the opposite effect, almost independent of horizontal resolution: Whereas the atmosphere is colder at low and middle latitudes, it is warmer at high latitudes and close to the surface. In addition, increased vertical resolution results in a pronounced warming in the polar upper troposphere and lower stratosphere where the cold bias is reduced by up to 50% compared to L19 simulations. Consistent with these temperature changes is a decrease and equatorward shift of the mid-latitude westerlies. The substantial benefits in refining both horizontal and vertical resolution are in accord with scaling arguments deduced from quasi-geostrophic theory implying that horizontal and vertical resolution ought to be chosen consistently.

1. Introduction

Earlier studies on the sensitivity of simulated climate to increased spatial resolution focused essentially on the following aspects:

- (i) At which resolution, if any, do the numerical solutions converge to an asymptotic state?
- (ii) Is there convergence towards a more realistic climate state?
- (iii) Independent of convergence, are there certain aspects of simulated climate or individual processes that are more realistically captured at higher resolution?

Answering these questions is not only of scientific interest but also of practical value because it would provide a rationale for choosing a suitable resolution for the particular model. The first question has been addressed in different model configurations. Boer and Denis (1997), in experiments with prescribed idealized forcing, i.e., excluding interactions between the dynamical and the physical (parameterized) part of the model, found convergence of the large-scale patterns around T63 spectral resolution. Williamson (1999) obtained more mixed results when studying features such as mid-latitude transients and the local Hadley circulation.

When the forcing was held fixed at T42 resolution, convergence of transient features were found only at lower wavenumbers ($\leq T42$). There was neither convergence at the higher wavenumbers nor in the full model due to the creation of finer scales interacting with the unresolved physics through latent heat release and convection. The strength of the Hadley circulation increased systematically up to the highest horizontal resolution applied (T170). These conclusions are in contrast to those obtained from numerous studies on the resolution dependence of the large-scale aspects of simulated climate. For example, Williamson et al. (1995) found convergence in zonal means, horizontal distributions and transient eddy statistics in the range T42 to T63. As compared to the differences T42-T21, the differences in the horizontal distributions of wind, geopotential height and sea level pressure were relatively small between T42 and T106. Similar conclusions were drawn by Boyle (1993), Déqué et al. (1994) and Stendel and Roeckner (1998). On the other hand, Boville (1991) found no evidence for convergence at T42. In fact, many of the changes between T63 (the highest resolution applied) and T42 were larger than those between T42 and T31. With respect to clouds, the convergence properties are model dependent. Kiehl and Williamson (1991) and Williamson et al. (1995) found a monotonous decrease of total cloud cover with increasing horizontal resolution up to T106, whereas Tiedtke (1993) reported little change except for a marked increase at higher vertical resolution (T63L31 vs. T63L19). In a very different model setup, Tompkins and Emanuel (2000) studied the impact of vertical resolution on the radiative-convective equilibrium in the tropics by means of single-column models driven by prescribed surface fluxes and radiative cooling. Convergence of the profiles of humidity and temperature was achieved at a resolution of around 25 hPa which is roughly half of the vertical grid distance employed in most current general circulation models.

Concerning the second question, numerous studies confirm the substantial reduction of systematic errors in medium-resolution models (T42, T63) compared to low-resolution models (T21, R15). This applies not only to seasonal mean climate but in particular to transient features such as eddy fluxes and processes like extratropical cyclones or blocking events. With respect to higher horizontal resolution (beyond T63) the conclusions differ between models and also depend on the climate statistics investigated. Some of the differences in model behavior at high resolution may also be attributed to the fact that in the early studies (before 1998) the simulation time was generally too short to obtain reliable climate statistics. As noted above, the differences in seasonal mean climate between T42 and T106 are generally much smaller than those between T42 and T21 (e.g., Boyle et al., 1993; Phillips et al., 1995). Nevertheless, some differences can be identified which may improve or deteriorate the simulation, depending on the simulated climate in the coarser resolution model. Increasing the horizontal resolution from T42 to T106 increased the tropospheric temperatures, predominantly at mid-latitudes, resulting in a poleward shift and intensification of the westerly jets (Boyle, 1993; Déqué et al., 1994; Pope and Stratton, 2002; Stendel and Roeckner, 1998; Stratton, 1999; Williamson et al., 1995). This extra

warming was caused mainly by latent heat release due to an intensification of the hydrological cycle (Pope and Stratton, 2002). Whereas the warming was often beneficial because some models suffered from a cold bias at coarse resolution, the poleward shift and intensification of the westerlies generally increased the systematic errors in high resolution experiments. Stratton (1999) showed that the Root-Mean-Squared-Error (RMSE) in sea level pressure increased at higher resolution, although some regional features improved such as a reduction of the high pressure bias over the Arctic. A steady increase with resolution (T30, T42, T106) in the RMSE of zonal mean climate variables was also found by Stendel and Roeckner (1998). On the other hand, the respective stationary wave components improved slightly at higher resolution. Intraseasonal variability tends to increase with increasing horizontal resolution. Transient eddy fluxes were underestimated at T42 and marginally overestimated at high resolution (Stendel and Roeckner, 1998; Stratton, 1999).

The deterioration with increasing horizontal resolution of some aspects of simulated climatology points to deficiencies in numerical schemes and/or parameterized physics, resolution dependence of parameterizations, or inadequate vertical resolution. An example of missing physics which became apparent at higher resolution in earlier models was the unrealistic zonalization of the northern hemisphere flow in models that did not employ dissipation through breaking gravity waves (Palmer et al., 1986). When this process was parameterized the zonalization problem was much less pronounced and the differences between low and high resolution became smaller (Boer and Lazare, 1988). Insufficient tuning of high resolution models due to the large computational costs may also contribute (Stendel and Roeckner, 1998), and inadequate vertical resolution is an issue as well (Lindzen and Fox-Rabinowitz, 1989; Pope et al., 2001; Tompkins and Emanuel, 2000). On the basis of quasi-geostrophic theory Lindzen and Fox-Rabinowitz (1989) concluded that vertical and horizontal resolution should be chosen ‘consistently’ to avoid a misrepresentation of horizontal and vertical scales, respectively. According to this argument vertical resolution should be enhanced together with increased horizontal resolution. At higher vertical resolution (30 levels instead of 19) Pope et al. (2001) found a substantial improvement in the temperature and moisture distribution in the upper troposphere and lower stratosphere. Using the same 30-level model, Pope and Stratton (2002) found a monotonous decrease of systematic errors in all dynamical quantities, unlike in earlier studies cited above, by increasing the horizontal resolution from $2.5^{\circ} \times 3.75^{\circ}$ (corresponding to T42) to $0.833^{\circ} \times 1.25^{\circ}$ (corresponding to T106).

Although higher resolution will not automatically reduce the systematic errors, there are indications that some individual processes are better captured at higher horizontal resolution. This includes features of the Indian and East Asian summer monsoon such as the rainfall pattern over the Indian subcontinent, the onset, temporal evolution and high-frequency characteristics of the summer monsoon (Sperber et al., 1994), or the position and strength of the Somali jet (Stephenson et al., 1998). High horizontal and vertical resolution is particularly important in the tropics. For example, tropical

cyclones which could hardly be resolved at T42 resolution were well captured in a T106 model simulation with respect to structure and frequency of occurrence (Bengtsson et al., 1995). High vertical resolution seems to be a necessary condition for a good simulation of other processes in the tropics like the Quasi-Biennial Oscillation (QBO) and the Madden-Julian Oscillation (MJO). Giorgetta et al. (2002) were able to capture both amplitude and period of the QBO realistically in a T42L90 simulation with a vertical grid spacing in the stratosphere ranging between 700 m and 1 km. A coarser resolution, with a grid spacing between 1.5 and 3 km in the stratosphere, was not sufficient for simulating the QBO. Inness et al. (2001) found an improved simulation of the MJO at higher vertical resolution (L30 vs. L19). This was attributed to a better representation of processes in the snow melt layer (around 600 hPa) favouring the occurrence of intermittent deep (mid-level) convection during active (suppressed) phases of the MJO.

The main objective of this study is to investigate the dependence of convergence properties and systematic errors on the vertical resolution. This is assessed in a series of AMIP-style experiments (Gates et al., 1999) at horizontal/vertical resolutions ranging between T21L19 and T159L31. Simulated seasonal mean climate variables are compared to those derived from the European Centre for Medium-Range Weather Forecasts (ECMWF) Reanalyses (ERA-15; Gibson et al., 1997). The model components are briefly summarized in section 2, and the experiments are described in section 3. The results are discussed in section 4. Section 5 contains a summary of the main findings and the concluding remarks.

2. Model components and surface data

A comprehensive model description of ECHAM5 is given by Roeckner et al. (2003; R2003 hereafter). Its main components are summarized as follows.

a. Dynamical core

Like its predecessors ECHAM1-4 (Roeckner et al., 1992; 1996), ECHAM5 employs a spectral dynamical core. Vorticity, divergence, temperature and the logarithm of surface pressure are represented in the horizontal by a truncated series of spherical harmonics. The general form of the corresponding equations follows that of the early multi-level spectral models (e.g., Hoskins and Simmons, 1975). Triangular truncation is used at wavenumbers 21, 31, 42, 63, 85, 106 or 159. The model utilizes a semi-implicit leapfrog time differencing scheme. The growth of spurious computational modes is inhibited by a weak time filter. A hybrid coordinate system is used in the vertical direction: The sigma system at the lowest model level gradually transforms into a pressure system in the lower stratosphere. In the standard configuration, the uppermost computational level is at 10 hPa with a total of either 19 or 31 levels. In the middle-atmosphere version the computational domain is extended to 0.01 hPa with either 39 or 90 levels. A second-order energy and angular momentum conserving scheme is used for finite differencing in the vertical (Simmons and Burridge, 1981).

b. Advective tracer transport

A flux-form semi-Lagrangian scheme (Lin and Rood, 1996) is used for passive tracer transport, i.e., for the water components (vapor, liquid, solid) and for chemical substances (optional). This type of advection scheme combines typical features of Eulerian flux-form schemes like exact mass conservation (to machine precision) with the unconditional stability for Courant numbers > 1 typical of non-conservative semi-Lagrangian schemes. Although the one-dimensional flux operators are guaranteed to be monotonic, this in general does not ensure that the full multi-dimensional scheme is monotonic as well. Furthermore, it has to be noted exact mass conservation is violated by a lack of consistency with the continuity equation which is solved within the spectral framework.

c. Physical parameterizations

Shortwave radiation

The scheme used in ECHAM5 for calculating radiative transfer of solar energy within the atmosphere (Fouquart and Bonnel, 1980) uses the Eddington approximation for the integration over the zenith and azimuth angles and the delta-Eddington approximation for the reflectivity of a layer. The scheme includes Rayleigh scattering, absorption by water vapor and ozone, both varying in space and time, and $\text{CO}_2 + \text{N}_2\text{O} + \text{CO} + \text{CH}_4 + \text{O}_2$ as uniformly mixed gases. Aerosols and cloud particles are effective through absorption and scattering. Interactions between scattering processes and absorption are considered for water vapor and for the uniformly mixed gases, but not for ozone, because gaseous absorption is assumed to dominate in the stratosphere. The computation of transmissivities and reflectivities across a vertical column is split into two separate calculations for the cloud-free part and the cloudy part. The scheme has four spectral bands, one for visible+UV range, and three for the near infrared. The interaction of scattering processes and gaseous absorption is considered only in the near infrared bands. Single scattering properties of clouds have been determined on the basis of Mie calculations using idealized size distributions for both cloud droplets and ice crystals (Rockel et al., 1991). For each of the 4 spectral intervals polynomial fits were derived allowing to express the respective single scattering properties as functions of the effective radii (R2003, Table 11.5) which are parameterized in terms of the liquid and ice water content, respectively.

Longwave radiation

The scheme implemented in ECHAM5 is the so-called ‘Rapid Radiative Transfer Model’ (RRTM) developed by Mlawer et al. (1997) based on the correlated-k method. Absorption coefficients have been derived from the LBLRTM line-by-line model (Clough et al., 1989, 1992; Clough and Iacono, 1995) and include the effect of the CKD2.2 water vapor continuum (Clough et al., 1989). The RRTM scheme computes

fluxes in the spectral range 10 cm^{-1} to 3000 cm^{-1} . The computation is organized in 16 spectral bands and includes line absorption by H_2O , CO_2 , O_3 , CH_4 , N_2O , CFC-11, CFC-12 and aerosols. Aerosols are considered in all spectral bands. The water vapor self continuum is taken into account in the troposphere only, the foreign continuum in the full column, though in bands 1 to 3 only (see R2003; Table 11.6). For cloud droplets, the mass absorption coefficient is a function of the respective effective radius with coefficients independent of wavenumber as obtained from a polynomial fit to the results of Mie calculations. For ice clouds, the parameterization of Ebert and Curry (1992) is used. Here, an inverse dependency of the mass absorption coefficient on the ice crystal effective radius is assumed, and the coefficients vary with wavenumber (see R2003; Tables 11.7, 11.8).

Stratiform cloud scheme

The scheme consists of prognostic equations for the water phases (vapor, liquid, solid), bulk cloud microphysics (Lohmann and Roeckner, 1996), and a statistical cloud cover scheme with prognostic equations for the distribution moments (Tompkins, 2002). The microphysics scheme includes phase changes between the water components (condensation/evaporation, deposition/sublimation, freezing/melting), and precipitation processes (autoconversion, accretion, aggregation). Moreover, evaporation of rain and melting of snow are considered as well as sedimentation of cloud ice. Subgrid-scale cloud formation is assumed to be caused solely by fluctuations in total water content which is represented by its probability density function (PDF; here: beta distribution). The variance of the total water content is obtained from the numerical solution of the respective prognostic equation, including production, turbulent transport and dissipation of variance, but neglecting advective transport. Changes in skewness are due to convective detrainment, as a source of positive skewness, cloud microphysics and dissipation that tends to relax a skewed distribution to a symmetric one.

Cumulus convection

A mass flux scheme is employed for shallow, mid-level and deep convection (Tiedtke, 1989) with modifications for deep convection according to Nordeng (1994). The scheme is based on steady state equations for mass, heat, moisture, cloud water and momentum for an ensemble of updrafts and downdrafts including turbulent and organized entrainment and detrainment. Turbulent entrainment and detrainment rates are specified differently for the three types of cumulus convection. Organized entrainment (for deep convection only) takes place as inflow of environmental air into the cumulus updraft when the cloud parcels accelerate upwards, that is, when the buoyancy is positive. Organized detrainment occurs where the air parcels decelerate, that is, when the buoyancy becomes negative. Thus, organized entrainment and detrainment is related to cloud activity itself. Cloud water detrainment in the upper part of the convective updrafts is used as source term in the stratiform cloud water equations. For deep convection, an adjustment-type closure is used with convective activity being expressed in terms of convective available potential energy (CAPE).

The cloud base mass flux is calculated by assuming that CAPE is relaxed towards zero over a specified time scale (typically one hour, but depending on horizontal resolution, see R2003).

Subgrid-scale orography effects

The subgrid-scale orography parameterization (hereafter SSOP) developed by Lott and Miller (1997) and Lott (1999) takes into account two main mechanisms of interaction between subgrid-scale orography and the atmospheric flow: (1) momentum transfer from the earth to the atmosphere accomplished by orographic gravity waves and (2) the drag exerted by the subgrid-scale mountain when the air flow is blocked at low levels. The part of the SSOP concerning propagation and dissipation of orographic gravity waves follows the formulation of Palmer et al. (1986) and Miller et al. (1989). In addition, the SSOP has options for including the effects of low-level trapped lee waves and of subgrid-scale orographic lift (Lott, 1999). Concerning the specification of the gravity wave forcing, the SSOP includes a relatively detailed description of the subgrid-scale orography (see section 2d and R2003).

Momentum flux deposition from a gravity wave spectrum

This parameterization, which is used only in the middle-atmosphere version of ECHAM5, is based on the Doppler spread theory of propagation and dissipation of a gravity wave spectrum (Hines, 1997). The forcing mechanisms generating the gravity waves are most likely located in the troposphere and may include convective activity, shear instability, frontal systems or transient flow over topography. In the middle atmosphere, the gravity waves propagate predominantly upward from their source regions, and they appear to form a broad background spectrum of waves. The quantity of interest is the deposition of the horizontal momentum transferred by the vertically propagating gravity waves. According to the Hines parameterization, the momentum flux deposition is obtained as a function of the input gravity wave spectrum, the buoyancy frequency and the horizontal wind (for details see Manzini et al., 1997 and R2003).

Horizontal diffusion

Unlike the other physical parameterizations, that are computed in grid point space, the horizontal diffusion is formulated in spectral space. It is expressed here in the form of a scale selective hyper-Laplacian applied to vorticity, divergence and temperature. Free parameters are the order of scheme and the diffusion coefficient or, alternatively, the e-folding damping time of the highest resolvable wavenumber. In ECHAM5, these parameters depend on the horizontal resolution (see R2003, Table 4.1). Furthermore, to avoid spurious wave reflection at the upper boundary, the damping is enhanced in the upper layers by gradually decreasing the order of the scheme.

Surface fluxes and vertical diffusion

The turbulent surface fluxes for momentum, heat and moisture are obtained from bulk transfer relationships involving the difference of the respective model variable (wind

components, potential temperature, humidity) between the surface and the lowest model level (about 30m above ground), the wind velocity at that level and the transfer coefficients. The latter are obtained from Monin-Obukhov similarity theory by integrating the flux-profile relationships between the surface and the lowest model level. Approximate analytical expressions in terms of roughness length and bulk Richardson number, similar to those suggested by Louis (1979), are employed for momentum and heat, respectively. Over land, the roughness length is a function of subgrid-scale orography and vegetation. Over sea, the aerodynamic roughness depends on friction velocity (Charnock, 1955), whereas the roughness length for heat transfer has to be adjusted owing to the fact that the transfer coefficient is largely independent of wind speed (Large and Pond, 1982). In unstable conditions, an interpolation is used between the free convection limit and the neutral approximation (Miller et al., 1992). Over land, transpiration is limited by stomatal resistance, and bare soil evaporation is limited by the availability of soil water. Above the surface layer the eddy diffusion method is applied. Eddy viscosity and diffusivity are parameterized in terms of turbulent kinetic energy (TKE) and length scales involving the mixing length and stability functions for momentum and heat, respectively (R2003). To determine TKE a simplified prognostic equation is solved neglecting both horizontal and vertical TKE advection and also horizontal diffusion (Brinkop and Roeckner, 1995).

Land surface processes

The surface temperature is obtained from the surface energy balance equation using an implicit coupling scheme that is unconditionally stable and allows to synchronously calculate the respective prognostic variables and surface fluxes (Schulz et al., 2001). To avoid iterations, the nonlinear terms appearing in the flux formulations, i.e., upward longwave radiation and the saturated specific humidity, are replaced by truncated Taylor expansions. The surface temperature is used as boundary condition to determine the vertical profile within the 5-layer soil model assuming vanishing heat fluxes at the bottom (10m). For snow covered land a mass-weighted mixture of soil and snow is applied to determine the thermal properties. Four reservoirs are defined for the water components: (1) snow at the canopy, (2) snow at the surface, (3) liquid water at the canopy, and (4) soil water. Surface runoff and drainage are obtained from a scheme which takes into account the heterogeneous distribution of field capacities within a grid-cell (Dümenil and Todini, 1992). For diagnostic purposes and for coupling to an ocean model, a hydrological discharge model is applied (Hagemann and Dümenil-Gates, 2001). A simple scheme is used for calculating the water temperature, ice thickness and ice temperature of lakes. Changes in water level are not considered. The albedo of snow and ice is assumed to be a linear function of surface temperature, ranging between a minimum value at the melting-point and a maximum value for ‘cold’ temperatures (see R2003; Table 6.1). Over snow covered land the mean albedo of a grid-cell depends on parameters like fractional forest area, leaf area index, bare soil albedo, snow albedo, fractional snow cover at both ground and canopy and slope of terrain (Roesch et al., 2001; R2003).

d. Land surface parameters

The dataset of land surface parameters utilized in ECHAM5 has been compiled by Hagemann (2002) from a global distribution of major ecosystem types that was made available by the U.S. Geological Survey. These parameters are the background albedo of snow-free land (with corrections for the Sahara desert according to satellite data), vegetation effect on roughness length (in addition to that of subgrid-scale orography), fractional vegetation cover, fractional forest cover, leaf area index, plant available and total soil water holding capacity. Most of these parameters are based on annual means. Exceptions are vegetation cover and leaf area index for which a seasonal cycle has been constructed. The basic resolution is 1km. Aggregation is done onto the respective model resolution. Furthermore, the orographic parameters (grid-cell mean as well as standard deviation, anisotropy, slope, orientation, minimum and maximum in the respective grid-cell) are obtained from the high-resolution (10' x 10') U.S. Navy topographic dataset. For snow-free land the volumetric soil heat capacity and thermal conductivity is prescribed for five soil types according to the FAO soil map.

3. Resolution experiments

A series of AMIP-style experiments (Gates et al., 1999) was performed using observed monthly sea surface temperatures and sea-ice cover for the time period 1978-1999. The output of the first year of each experiment was omitted. A seasonal climatology (DJF, MAM, JJA, SON) was constructed from the 15-year period 1979-1993 and compared with the respective ERA-15 dataset (Gibson et al., 1997) covering the same period. Except for model tuning (see below), the experiments differ only with respect to horizontal and/or vertical resolution. Although there is only one realization for each resolution experiment, this appears to be sufficient because the focus is on the systematic errors of the simulated time-mean state in basic dynamical quantities like temperature, wind, geopotential height and sea level pressure. For example, the differences in model climatologies between the full period (until 1999) and the ERA-15 compatible subset (until 1993), are negligibly small compared to those between the model climatologies and the ERA-15 data. Hence, the sampling size should not be an issue in this study. A list of the resolution experiments together with the respective top-of-atmosphere radiative fluxes is presented in Table 1. The L19 vertical grid is identical to that used in previous ECHAM models, the L31 grid is identical to that used in the ERA-15 model (see R2003, Table 2.2). In all experiments the top level is placed at 10 hPa. The top three and the bottom three levels are identical in both grids. In the L19 (L31) model the geometrical grid spacing in the free troposphere increases gradually with height from about 1km (500m) in the lower troposphere, to 1.5km (750m) in the middle troposphere, and 2km (1km) around the tropopause.

Except for a few parameter changes, the physical package remains identical. Some of the parameter changes are directly linked to resolution changes as, for instance, the damping time of the highest resolvable wavenumber in the horizontal diffusion

scheme, the subgrid-scale parameters in the orographic drag scheme or the adjustment time scale utilized in the penetrative convection parameterization. Other parameters had to be tuned in order to approximately satisfy the long-term mean net radiation balance at the top of the atmosphere. This has been achieved by modifying free parameters in the cloud and convection schemes, which affect precipitation efficiency and, hence, cloud cover, cloud water content and cloud radiative forcing. A similar strategy was applied by Williamson et al. (1995), Stendel and Roeckner (1998) and Pope and Stratton (2002). As apparent from Table 1, there is no resolution dependence of the shortwave clear-sky fluxes, but some effect on the clear-sky OLR, with systematically larger fluxes, up to 3.6 W/m^2 , at higher horizontal horizontal and especially at higher vertical resolution. Because of inaccuracies of radiometers, sampling errors and other factors, the net clear-sky flux in the ERBE data ($+24 \text{ W/m}^2$) is not compensated by the net cloud-radiative effect which is -18 W/m^2 . To achieve a net radiation budget closer to zero in the simulations (last column), the net cloud-radiative forcing has been systematically shifted to more negative values compared to the satellite data, distributed almost equally between the SW cloud-radiative cooling, which is always larger than in ERBE, and the LW cloud-radiative warming which is smaller.

4. Results and Discussion

a. Root-Mean-Squared-Errors (RMSE)

The RMSE were calculated from the differences between simulated seasonal climatologies from the respective ERA-15 data for the period 1979-1993. This includes basic climate variables like temperature, geopotential height and zonal wind in the upper troposphere (200 hPa), middle troposphere (500 hPa) and lower troposphere (850 hPa). In addition, the RMSE of mean sea level pressure has been calculated. Table 2 shows the respective values averaged over all four seasons. In most cases the errors decrease with increasing horizontal resolution. However, there are a few exceptions, most notable Z200 and Z500 in the L19 simulations: Whereas these errors decrease between T21 and T42, they increase steadily between T42 and T106.

In the L31 simulations there is virtually no evidence for such an anomalous behavior. With the exception of a small increase of the T500 and T850 errors in T106L31 and T159L31, there is a monotonous decrease of RMSE with increasing horizontal resolution. Moreover, the L31 simulations are generally substantially closer to ERA-15 than their L19 counterparts (Table 3). A notable exception is the T42 model where a better vertical resolution does not improve the simulation. For 50% of all variables analyzed here the T42L31 errors are larger than those of T42L19. In the T63, T85, and T106 simulations the beneficial effect of higher vertical resolution is particularly evident for Z200 and Z500, but improvements are found for the other variables and levels as well. The only exception is the zonal wind at 200 hPa which is too strong at low latitudes in the L31 simulations.

Based on the numbers shown in Table 2, a simple ranking scheme was designed by calculating the ratio of the respective RMSE and those from the T21L19 simulation, and averaging these normalized errors over all variables and levels. This was done separately for the total fields (Fig. 1a), for the zonal means (Fig. 1b) and also for the stationary wave components (Fig. 1c). In the L19 simulations (left columns), in agreement with most earlier studies (see section 1), there is no evidence for an overall decrease in total error for resolutions higher than T42, but there are significant improvements from T21 to T31 and also from T31 to T42. Increased vertical resolution (right columns) is beneficial in two aspects. Firstly, the errors are smaller than their L19 counterparts (except for T42) by up to 17% for T106. Secondly, the errors decrease monotonously with increasing horizontal resolution up to the highest horizontal resolution applied in this study (T159). This is in qualitative agreement with the results obtained by Pope and Stratton (2002) from HadAM3 simulations at higher vertical resolution (L30). The improvements in the L31 simulations compared to L19 are more pronounced in the zonal means (up to 20% decrease in normalized error, see Fig. 1b) than in the stationary waves (up to 6% decrease, see Fig. 1c). This is expected because stationary wave amplitudes are relatively small except in boreal winter. In agreement with ECHAM4 L19 results (Stendel and Roeckner, 1998) the stationary wave errors, at both vertical resolutions, decrease monotonously with increasing horizontal resolution.

b. Zonal means

Latitude-height cross sections of DJF zonal mean temperature errors in L19 simulations are shown in Fig. 2. As in virtually all earlier studies, higher horizontal resolution results in a gradual tropospheric warming. In some regions this extra warming is beneficial because a cold bias at lower resolution is diminished as, for example, the cold bias in the lower troposphere and at high latitudes in the T42 simulation. In other regions the systematic errors increase because a warm bias already present at lower resolution is enhanced. This is particularly evident in the middle troposphere (see also Table 2) at low and middle latitudes. The warm bias increases steadily between T42 and T85 with some indication of convergence at this resolution though not in all regional details.

In the respective L31 simulations (Fig. 3) an overall cold bias prevails. As in L19, there is a gradual warming with increasing horizontal resolution in much of the troposphere. The difference pattern (L31-L19) in zonal mean DJF temperature (Fig. 4) is largely independent of horizontal resolution. The most notable features are cooling of the middle and upper troposphere at low and middle latitudes, and high-latitude warming, most pronounced between 200 and 100 hPa. Almost all of these changes are beneficial (see also Table 2) and remarkably similar to those found by Pope et al. (2001) in HadAM3 simulations. Oppositely, Williamson and Olsen (1998) obtained

high-latitude cooling of the tropopause and lower stratosphere when vertical resolution was increased.

As shown in Fig. 5, the evolution of the warm bias in the L19 simulations is even more evident during JJA with values exceeding 2°C at T85 and T106 resolution in parts of the summer hemisphere. In the L31 simulations (Fig. 6), a warm bias in parts of the troposphere is evolving, but this is smaller by typically 50% compared to L19. As shown in Fig. 7, the impact of increased vertical resolution is similar to that in DJF (Fig. 4) and beneficial throughout the domain: Compared to L19 there is less warming at low and middle latitudes, less cooling at high southern latitudes and, in particular, a substantial reduction of the cold bias in the polar upper troposphere and lower stratosphere. In T159L31 (Fig. 8) the error patterns are generally similar to those of T106L31 (see Figs. 3 and 6). In much of the troposphere the differences (T159-T106) are smaller than 0.5K. Larger changes are found in the polar upper troposphere and lower stratosphere where the T159 temperatures are systematically higher compared to T106. Noteworthy is the DJF warm bias over the North Pole (relative to ERA-15), which is in contrast to the respective error patterns at lower horizontal resolution (see Fig. 3). This sign reversal is probably caused by an overly strong gravity wave drag (no attempt was made to optimize the parameters at this resolution). In the respective summer hemisphere the gravity wave drag is relatively unimportant. Therefore the decrease of the cold polar bias around 200 hPa in the T159L31 simulation compared to T106L31 (more than 1K in DJF over the South Pole and more than 2K in JJA over the North Pole) is more likely due to the increase in horizontal resolution (see also the decrease in RMSE at this level: Table 2, first column).

Figure 9 shows the impact of horizontal resolution on DJF zonal wind errors in the L19 simulations. From T42 to T85 there is a gradual evolution of a pattern found in many earlier resolution studies (see section 1), that is, an unrealistic poleward shift of the mid-latitude westerlies throughout the troposphere, especially in the southern hemisphere. However, there is no evidence for a further deterioration at T106 resolution. In the northern hemisphere, an improvement is found compared to T85, and the T106 pattern is actually similar to that of T63. A beneficial effect of increased horizontal resolution can be identified in the middle and upper tropical troposphere. Here, the westerly wind bias evident at T42 resolution is gradually diminished at higher resolution.

In the L31 simulations (Fig. 10) the impact of increased horizontal resolution on zonal wind is similar to L19, but the error patterns differ considerably between L19 and L31. For example, in the T42L31 simulation, the error between 30°S and 70°S reflects an equatorward shift and weakening of the westerlies. As horizontal resolution is increased, this error becomes less pronounced until it practically disappears at T106 resolution. Higher vertical resolution tends to reduce the mid-latitude westerly wind bias above 200 hPa, whereas the upper tropospheric westerly bias in the tropics is more pronounced than in the L19 simulations. As for temperature, the impact of

increased vertical resolution on zonal wind (Fig. 11) is largely independent of horizontal resolution. Consistent with the respective temperature changes (Fig. 4), the mid-latitude westerlies move equatorward and weaken. This is more pronounced in the southern hemisphere than in the northern hemisphere. Easterly components, relative to L19, are simulated throughout the stratosphere, whereas westerlies occur in the upper tropical troposphere. These changes are again very similar to those found by Pope et al. (2001). Most of the changes (L31-L19) are beneficial at sufficiently high horizontal resolution (\geq T63).

Figure 12 shows JJA errors in zonal mean zonal wind in the L19 simulations. The northern hemisphere westerlies are always too strong, and the impact of increasing horizontal resolution is only modest. In the T42 simulation, the southern hemisphere westerlies are too weak and shifted equatorward. As the resolution is increased, the errors become smaller and almost vanish at T85 and T106 resolution. Also, as in DJF, the westerly wind bias in the middle and upper tropical troposphere decreases with increasing horizontal resolution.

At higher vertical resolution (Fig. 13) an overall improvement compared to the L19 simulations is not so clear. Whereas the westerly bias centred around 50°N is reduced, the easterly bias around 60°S is indicative for decreased westerlies at the poleward flank of the jet. Although the easterly bias is less pronounced at higher horizontal resolution (T85, T106) it is larger than in the respective L19 simulations. Also, as in DJF, the westerly wind bias in the middle and upper tropical troposphere is larger than in the L19 simulations. On the other hand, the mid-latitude westerly bias above 200 hPa is reduced in the L31 simulations. The similar patterns at higher resolution suggest convergence around T85.

The differences in JJA zonal wind between the L31 and L19 simulations is shown in Fig. 14. Apart from details, the impact of horizontal resolution is relatively small, and the basic pattern is established already in the T42 simulations. As in DJF (Fig. 11), easterly components, relative to L19, are simulated in the stratosphere and on the poleward flanks of the tropospheric westerlies. On the other hand, westerlies are found at lower latitudes with maxima of up to 5 m/s below the tropical tropopause, enhancing the westerly wind bias relative to L19. In T159L31 (Fig. 15), most of the errors seen in T106L31 can be found as well. An exception is the weakening of the DJF polar night jet, relative to both ERA-15 and T06L31, which is consistent with the presumption of an overly strong gravity wave drag (as discussed earlier).

Zonal mean errors of 500 hPa geopotential height and sea level pressure are shown in Fig. 16 for DJF and JJA, respectively. In general, increased vertical resolution, from L19 to L31, has a substantially bigger impact than the increase in horizontal resolution from T63 to T106. In the L19 simulations a positive bias in Z500 is found throughout the domain, with the exception of high southern latitudes during DJF: The positive (negative) biases in both Z500 and SLP between 30°S and 60°S (60°S and 90°S) is

consistent with the westerly wind bias in the L19 simulations centred around 60°S (c.f., Fig. 9). During JJA, the improvements in the L31 simulations are less systematic, and some deterioration, compared to L19, is found at high southern latitudes: The positive biases in both Z500 and SLP poleward of about 50°S are consistent with the easterly wind biases in the L31 simulations centred around 60°S (c.f., Fig. 13). In MAM the errors in the L31 simulation are relatively small and similar to DJF, whereas the SON errors resemble those of JJA (not shown).

c. Geographic distributions

A comparison of simulated DJF sea level pressure distributions (T106L19, T106L31) with ERA-15 is shown in Fig. 17. In both simulations the cores of the Icelandic and Aleutian lows are slightly underestimated but the respective positions are reasonably well captured, although the Icelandic low core in L19 is extended too far into the Norwegian Sea. The high pressure regimes are more realistically captured in the L31 simulation. For example, there is a better separation than in L19 of the three anticyclones over North America, East Atlantic/South Europe/North Africa, and Asia. In the southern hemisphere the simulated anticyclones over the Pacific, Atlantic, and Indian Ocean are somewhat weaker in the L31 simulations and in better agreement with the ERA-15 pattern compared to L19. The differences between L19 and L31 are more evident in the error patterns shown in Fig. 18. The improvements at L31 noticed already in the zonal means (Fig. 16) are obviously not due to error compensation along latitudes but can be found in almost every grid point.

In JJA (Fig. 19) the differences between the simulations are smaller than in DJF. At both resolutions the anticyclones over the North Pacific and North Atlantic are somewhat too strong whereas the respective patterns in the southern hemisphere are slightly better captured in the L31 simulation. On the other hand, the trough around Antarctica is deeper and also more realistic in the L19 simulation. This is evident from the respective error patterns shown in Fig. 20. In the northern hemisphere, on the other hand, the L31 errors are clearly smaller compared to L19. For example, the high pressure bias over the North Pacific, evident in L19, is significantly smaller in L31. Also the low pressure bias at high northern latitudes (< 3 hPa in L19) can hardly be found in the L31 simulation.

Stationary waves triggered by orography, land-sea contrast, but also influenced by transient eddies and dependent on the mean zonal flow are important features of the northern hemisphere climate in winter. Figure 21 shows a comparison between model simulations and ERA-15 of stationary wave patterns in 500 hPa geopotential height during DJF in the northern hemisphere. In the T106L19 simulation the ridge over the East Atlantic and Europe is well captured. In the other regions the simulation shows deficiencies which are typical for all L19 simulations. The amplitude of the West Pacific trough is well captured, but it is not far enough extended to the east. Most obvious is the underestimation of the ridge over the Rocky mountains and the

underestimation of the trough over the eastern part of North America. In the L31 simulations the stationary waves are captured more realistically. This applies to all features discussed above, except for the East Atlantic ridge which is somewhat too high compared to ERA-15. The superiority of the L31 simulations is clearly evident in the respective error patterns shown in Fig. 22. As for the variables discussed earlier, the impact of increased vertical resolution is larger than that of increased horizontal resolution. Some of the errors in the L19 simulations are no longer visible in the L31 simulations like, for example, the East Pacific/Rocky mountains anomalies, whereas some other features persist such as the slightly too high values in the center of the West Pacific and North American troughs and the low-pressure bias over parts of the North Atlantic and northern Europe. In general, however, the amplitude of these error patterns is considerably reduced by increasing the vertical resolution, especially in the T106L31 simulation.

d. Water vapor and cloud

The temperature differences between L31 and L19 simulations (see Figs. 4 and 7) are associated with changes in specific and relative humidity, cloud cover and cloud water content. Figure 23 shows the relative change (in %) of DJF specific humidity between the L31 and L19 simulations. A comparison with Fig. 4 indicates that some of the changes, but not all, may be directly linked with temperature changes. For example, the upper tropospheric drying at lower latitudes and the moistening at high latitudes may be regarded as a response to the respective temperature changes, assuming that the changes in relative humidity are small. Although this assumption is approximately fulfilled in the polar lower and middle troposphere, the relative humidity below the tropical tropopause decreases actually by about 10% in the L31 simulations (not shown). The decrease in relative humidity is even larger in the polar upper troposphere and lower stratosphere where the decline in specific humidity by up to 50% is accompanied by a warming of several degrees (Fig. 4). Here the drying is not simply a response to temperature changes. Very likely, the causality has to be reversed (M. Ponater, pers. comm.): In the previous model version, ECHAM4, the specific humidity around the 200 hPa level was up to 5 times higher compared to satellite data (HALOE) whereas the model was spuriously dry by up to 50% in the polar lower stratosphere. By ‘nudging’ the HALOE data into the ECHAM4 model, the cold polar bias was reduced by about 70% (i.e., by up to 8 K of its value in the control run). These results support the conclusion that the upper tropospheric drying at higher vertical resolution is the main reason for the reduced cold polar bias in the L31 simulations. The changes (L31-L19) in specific humidity and temperature are similar to those obtained by Pope et al. (2001) who found a dramatic improvement (i.e., a decrease) of upper tropospheric humidity at higher vertical resolution (L30 compared to L19) and a decrease of the cold polar bias due to reduced longwave cooling at these levels. The decrease in specific humidity at higher vertical resolution can be related to a better representation of the polar tropopause and hygropause, which are spuriously shifted upward at lower vertical resolution. Numerical diffusion inherent in the

transport algorithm for water vapor could be another contributing factor, that is, vertical humidity gradients can be better maintained at higher vertical resolution (see Fig. 23 and Fig. 10a of Pope et al., 2001).

The low-latitude difference (L31-L19) is more complex because, in addition to resolved processes, subgrid-scale processes like convection play a major role. Whereas the lower and middle troposphere is moister in the upward branch of the Hadley circulation, there is drying in the downward branches. These changes are consistent with a slight strengthening of the Hadley circulation in the L31 simulations (not shown). Noteworthy is the local maximum of moistening around 600 hPa for resolutions \geq T63. This is caused by a better representation of the melt layer. The extra cooling associated with snow melt causes a marked change in stability so that deep convective clouds are not able to easily penetrate this layer, as in the L19 model, but start detraining in the melt layer already (Tompkins and Emanuel, 2000; Inness et al., 2001). Analogously, the decrease in upper tropospheric humidity by typically 30% can partially be attributed to less frequent occurrence of deep convective clouds and the associated reduction of cloud top detrainment. Although moistening by mid-tropospheric convective detrainment was also identified in HadAM3 L30 simulations (Pope et al., 2001; Inness, 2001), this was masked by other processes so that drying relative to L19 was simulated throughout the low-latitude troposphere. Part of the differences can be related to the horizontal resolution used in these studies (equivalent to T42). In fact in our T42 simulation the moistening above 800 hPa is very small. In addition to convective detrainment, the vertical humidity transport by the resolved scales is an important humidity source in the middle and upper troposphere. Insufficient vertical resolution could result in excessive numerical diffusion in the advection scheme. Therefore, the upper tropospheric drying relative to L19 may be caused also by diminished vertical transport due to less artificial diffusion (Pope et al., 2001). The ECHAM5 and HadAM3 results agree qualitatively with those obtained in single-column model studies by Tompkins and Emanuel (2000), who showed that convergence of humidity and temperature profiles in the tropics can be achieved at a vertical resolution of about 25 hPa. At lower resolution (50 hPa), comparable to our L19, the humidity was spuriously high compared to the converged value by up to 30% in the upper half of the troposphere, and the temperature was also higher by up to 5 K than at 25 hPa resolution.

Most of the differences (L31-L19) in DJF specific humidity can also be found in the JJA season (Fig. 24). The largest decrease (by more than 50% for resolutions \geq T63) occurs over the summer pole, just above the 200 hPa level. Also, as in DJF, there is widespread drying in the upper troposphere and lower stratosphere, except for the region poleward of 60°S, and a moistening (drying) in the upward (downward) branches of the Hadley circulation in the lower and middle troposphere. In JJA there is a larger hemispheric asymmetry than in DJF. In the southern hemisphere the moistening poleward of 30°S extends up to 400 hPa and higher poleward of 60°S. In

the northern hemisphere the extratropical moistening is confined to the lower levels, especially at high horizontal resolution (T85, T106).

As for humidity, the differences (L31-L19) in DJF and JJA cloud cover shown in Figs. 25 and 26 are largely independent of horizontal resolution. Cloud cover decreases by up to 10% in the upper levels but also in the boundary layer. Cloud cover increases predominantly in the mid-troposphere with maxima of more than 3% at mid-latitudes and in the upward branch of the Hadley circulation. Here, as for specific humidity (Fig. 23), a local maximum in the snow melt layer (600 hPa) is generated. As to be expected the differences in cloud cover are broadly consistent with those in cloud ice (Figs. 27 and 28). The overall decrease at higher levels and the increase below are indicative of a downward displacement of the tropopause at higher vertical resolution. In the tropics this is related to changes in the frequency distribution of convective clouds, that is, mid-level detrainment is enhanced at the expense of high-level detrainment. In addition to the respective humidity changes (Figs. 23 and 24), this contributes to a cooling relative to L19 (see Figs. 4 and 7) through enhanced cloud top radiative cooling in the mid-troposphere and reduced cloud radiative heating due to the decrease in high-level cirrus clouds. At high latitudes the decrease in cloud cover centred around 200 hPa is consistent with that in humidity. Both changes contribute to the warming relative to L19 through a decrease in longwave radiative cooling at these levels (e.g., Pope et al., 2001).

5. Summary and concluding remarks

The main objective of this study is to assess the dependence of systematic errors in basic climate variables to changes in both horizontal and vertical resolution. Other aspects of simulated climate which could be sensitive to resolution like, for example, transients in both the tropics and extratropics, interannual variability or the water cycle are beyond the scope of this study.

As in many earlier studies (e.g., Boville, 1991; Boyle, 1993; Déqué et al., 1994; Williamson et al., 1995, Stendel and Roeckner, 1998; Stratton, 1999; Pope and Stratton, 2002) increasing horizontal resolution leads to a warming of the troposphere, most prominently at mid-latitudes and, hence, to a poleward shift and intensification of the mid-latitude westerlies. Increasing the vertical resolution has the opposite effect, almost independent of horizontal resolution: Whereas the atmosphere is colder at low and middle latitudes, it is warmer close to the surface and at high latitudes, most pronounced in the polar upper troposphere and lower stratosphere where the cold polar bias is reduced by up to 50% compared to L19 simulations. Consistent with these temperature changes is a decrease and equatorward shift of the mid-latitude westerlies.

Higher vertical resolution leads to a marked redistribution of humidity and clouds. Most notable is the drying of the upper troposphere (centred around the 200 hPa level), which is related to a lowering of the tropopause and hygropause. Analyses by

Pope et al. (2001) and Ponater (2004, pers. comm.) suggest that decreased radiative cooling in the drier polar upper troposphere contribute to the decrease of the cold polar bias. In the tropics the humidity and cloud response to increased vertical resolution is related to changes in cloud top detraining of water vapor and cloud water/ice. In agreement with Inness et al. (2001), enhanced vertical resolution leads to better representation of the snow melt layer in the tropics and, hence, to more frequent occurrence of cumulus clouds detraining at this level. This is reflected in the local increase of both humidity and clouds in our L31 simulations. Associated with a higher frequency of mid-tropospheric cumulus congestus is a lower frequency of deep cumulus clouds. The reduced convective detraining contributes to the decline, relative to L19, of humidity and clouds in the tropical upper troposphere. The resulting upper tropospheric cooling and drying, and also the moistening in the boundary layer and in the snow melt layer, are qualitatively similar to the single-column model results obtained by Tompkins and Emanuel (2000) who stressed the need for sufficient vertical resolution (about 25 hPa) to correctly simulate the vertical profiles of humidity and temperature in the tropics.

The answers to the questions raised in section 1 depend on the vertical resolution used in the model. In the L19 simulations, as in most previous studies, there is little evidence for convergence to a more realistic climate state at horizontal resolutions $>$ T42. In the L31 simulations, on the other hand, the RMSE decrease monotonously with increasing horizontal resolution (T42 to T159). Furthermore, except for T42 horizontal resolution, the L31 versions are superior to their L19 counterparts, and the improvements become more evident at increasingly higher horizontal resolutions. This applies, in particular, to the zonal mean climate state but also to stationary wave patterns in boreal winter. The substantial benefits in refining horizontal and vertical resolution at the same time are in accord with scaling arguments deduced from quasi-geostrophic theory (Lindzen and Fox-Rabinovitz, 1989; Fox-Rabinovitz and Lindzen, 1993) implying that horizontal and vertical resolution ought to be chosen consistently. For quasi-geostrophic flows the Rossby ratio of horizontal and vertical scales is given by $L/H = N/f_0 \approx 100$ where N is the Brunt-Väisälä frequency and f_0 a characteristic Coriolis parameter. Lindzen and Fox-Rabinovitz (1989) also showed that the vertical resolution requirement is even more demanding for internal gravity waves. Table 4 compares the vertical grid spacing at 500 hPa in the L19 and L31 models with those derived from the consistency relationship at 45° for two choices of N corresponding to oscillation periods of 5 and 8 min, respectively. According to Table 4, L19 vertical resolution is adequate for T31 and T42, whereas L31 is adequate for T63 and T85. Even higher vertical resolution would be required for T106 and T159. It has to be pointed out, however, that this analysis can only provide a rough first hint for the proper choice of the vertical model resolution, because neither f_0 nor N are constants, and Δz in ECHAM5, as usual, varies with height: Within the troposphere there is a gradual increase of Δz from the top of the boundary layer up to the tropopause, with Δz shown in Table 4 representing approximately a free tropospheric mean (see also section 3).

It is important to note that by comparing just two vertical resolutions the convergence properties with respect to vertical resolution cannot be fully assessed. More systematic studies on this topic are required. Furthermore, although changes in resolution are mostly affecting the resolved scales, there is also an impact on the parameterized physics. Some of this impact has been minimized through model tuning in order to achieve, for example, a top-of-atmosphere radiation balance close to zero. For processes like orographic gravity wave drag there is no such rationale. The parameter choice is more subjective and based on a series of long test simulations which can easier be done at low resolution than at high resolution. In fact, the T159L31 simulation suffers partially from an overly strong orographic gravity wave drag.

In the past, increasing computer power has been used predominantly for increasing the horizontal resolution. According to our analyses, a more balanced choice of horizontal/vertical resolution does not only improve the performance of the model but is beneficial also from an economic point of view. A striking example is the T106L19 model in comparison to T63L31. The latter is not only more efficient in terms of CPU time (65% of T106L19) but also more accurate by more than 10% in terms of overall RMSE. A further gain in quality by 10% can only be achieved at very high cost (factor of 13 with respect to T63L31 in the T159L31 model). Here the choice of resolution would be more subjective because the lack of accuracy in T63L31 can be balanced by the advantages of longer simulation length and larger ensembles.

REFERENCES

- Bengtsson, L., M. Botzet, and M. Esch, 1995: Hurricane-type vortices in a general circulation model. *Tellus*, **47A**, 175-196.
- Boer, G.J. and B. Denis, 1997: Numerical convergence of the dynamics of a GCM. *Clim. Dyn.*, **13**, 359-374.
- Boer, G.J. and M. Lazare, 1988: Some results concerning the effect of horizontal resolution and gravity wave drag on simulated climate. *J. Climate*, **1**, 789-806.
- Boville, B.A., 1991: Sensitivity of simulated climate to model resolution. *J. Climate*, **4**, 469-485.
- Boyle, J.S., 1993: Sensitivity of dynamical quantities to horizontal resolution for a climate simulation using the ECMWF (cycle 33) model. *J. Climate*, **6**, 796-815.
- Bretagnon, P. and G. Francou, 1988: Planetary theories in rectangular and spherical variables – VSOP solutions. *Astronomy and Astrophysics*, **202**, 309-315.
- Brinkop, S. and E. Roeckner, 1995: Sensitivity of a general circulation model to parameterizations of cloud-turbulence interactions in the atmospheric boundary layer. *Tellus*, **47A**, 197-220.
- Charnock, 1955: Wind stress on a water surface. *Q. J. Roy. Meteor. Soc.*, **81**, 639-640.

- Clough, S.A. and M.J. Iacono, 1995: Line-by-line calculations of atmospheric fluxes and cooling rates. II. Application to carbon dioxide, ozone, methane, nitrous oxide and the halocarbons. *J. Geophys. Res.*, **100**, 16519-16536.
- Clough, S.A., M.J. Iacono, and J.-L. Moncet, 1992: Line-by-line calculations of atmospheric fluxes and cooling rates. Application to water vapor. *J. Geophys. Res.*, **97**, 15761-15786.
- Clough, S.A., F.X. Kneizys, and R.W. Davies, 1989: Line shape and the water vapor continuum. *Atmos. Res.*, **23**, 229-241.
- Déqué, M., C. Dreverton, A. Braun, and D. Cariolle, 1994: The ARPEGE/IFS atmosphere model: a contribution to the French community climate modelling. *Clim. Dyn.*, **10**, 249-266.
- Dümenil, L. and E. Todini, 1992: A rainfall-runoff scheme for use in the Hamburg climate model. In: J.O. Kane (Ed.) *Advances in Theoretical Hydrology, a Tribute to James Dooge*. European Geophysical Society Series on Hydrological Sciences, pp. 129-157. Elsevier, Amsterdam.
- Ebert, E.E. and J.A. Curry, 1992: A parameterization of cirrus cloud optical properties for climate models. *J. Geophys. Res.*, **97**, 3831-3836.
- Fortuin, J.P.F. and H. Kelder, 1998: An ozone climatology based on ozonesonde and satellite measurements. *J. Geophys. Res.*, **103**, 31709-31734.
- Fouquart, Y. and B. Bonnel, 1980: Computations of solar heating of the Earth's atmosphere: A new parameterization. *Beitr. Phys. Atm.*, **53**, 35-62.
- Fox-Rabinovitz, M.S. and R.S. Lindzen, 1993: Numerical experiments on consistent horizontal and vertical resolution for atmospheric models and observing systems. *Mon. Wea. Rev.*, **121**, 264-271.
- Gates, W.L., J.S. Boyle, C. Covey, C.G. Dease, C.M. Doutriaux, R.S. Drach, M. Fiorino, P.J. Gleckler, J.J. Hnilo, S.M. Marlias, T.J. Phillips, G.L. Potter, B.D. Santer, K.R. Sperber, K.E. Taylor, and D.N. Williams, 1999: An overview of the results of the Atmospheric Model Intercomparison Project (AMIP I). *Bull. Amer. Met. Soc.*, **80**, 29-55.
- Gibson, J.K., P. Kallberg, S. Uppala, A. Hernandez, A. Nomura, and E. Serrano, 1997: ERA description. ECMWF Reanalysis Project Report Series 1. European Centre for Medium-Range Weather Forecasts, Reading, United Kingdom, 72 pp.
- Giorgetta, M., E. Manzini and E. Roeckner, 2002: Simulation of the quasi-biennial oscillation from a broad spectrum of atmospheric waves. *Geophys. Res. Lett.*, **29**, 10.1029/2002GL014756.
- Hagemann, S, 2002: An improved land surface parameter data set for global and regional climate models. Report No. **336**, Max-Planck-Institut für Meteorologie, Hamburg, Germany, 21 pp.
- Hagemann S., L. Dümenil-Gates, 2001: Validation of the hydrological cycle of ECMWF and NCEP reanalyses using the MPI hydrological discharge model. *J. Geophys. Res.*, **106**, 1503- 1510.
- Hartmann, D., 1993: Radiative effects of clouds on Earth's climate. In: P.V. Hobbs (Ed.) *Aerosol-Cloud-Climate Interactions*, 151-173, Academic Press.

- Hines, C.O., 1997: Doppler spread parameterization of gravity wave momentum deposition in the middle atmosphere. Part I: Basic formulation. *J. Atmos. Terr. Phys.*, **59**, 371-386.
- Hoskins, B.J. and A.J. Simmons, 1975: A multi-layer spectral model and the semi-implicit method. *Q. J. Roy. Meteor. Soc.*, **101**, 637-655.
- Inness, P.M., J.M. Slingo, S.J. Woolnough, R.B. Neale, and V.D. Pope, 2001: Organising of tropical convection in a GCM with varying vertical resolution: implications for the simulation of the Madden-Julian Oscillation. *Clim. Dyn.*, **17**, 777-793.
- Kiehl, J.T. and K.E. Trenberth, 1997: Earth's annual global mean energy budget. *Bull. Amer. Met. Soc.*, **78**, 197-208.
- Kiehl, J.T. and D.L. Williamson, 1991: Dependence of cloud amount on horizontal resolution in the National Center for Atmospheric Research Community Climate Model. *J. Geophys. Res.*, **96**, 10955-10980.
- Large, W.G. and S. Pond, 1982: Sensible and latent heat flux measurements over the ocean. *J. Phys. Oceanogr.*, **12**, 464-482.
- Lin, S.J. and R. B. Rood, 1996: Multidimensional flux form semi-Lagrangian transport. *Mon. Wea. Rev.*, **124**, 2046-2068.
- Lindzen, R.S. and M.S. Fox-Rabinovitz, 1989: Consistent vertical and horizontal resolution. *Mon. Wea. Rev.*, **117**, 2575-2583.
- Lohmann, U. and E. Roeckner, 1996: Design and performance of a new cloud microphysics parameterization developed for the ECHAM4 general circulation model. *Clim. Dyn.*, **12**, 557-572.
- Lott, F., 1999: Alleviation of stationary biases in a GCM through a mountain drag parameterization scheme and a simple representation of mountain lift forces. *Mon. Wea. Rev.*, **127**, 788-801.
- Lott, F. and M.J. Miller, 1997: A new subgrid-scale orographic drag parameterization: Ist formulation and testing. *Q. J. Roy. Meteor. Soc.*, **123**, 101-127.
- Louis, J.-F., 1979: A parametric model of vertical eddy fluxes in the atmosphere. *Bound.-Layer Meteor.*, **17**, 187-202.
- Manzini, E., N.A. McFarlane, and C. McLandress, 1997: Impact of the Doppler spread parameterization on the simulation of the middle atmosphere circulation using the MA/ECHAM4 general circulation model. *J. Geophys. Res.*, **102**, 25751-25762.
- Miller, M.J., A. Beljaars, and T.N. Palmer, 1992: The sensitivity of the ECMWF model to the parameterization of evaporation from the tropical oceans. *J. Climate*, **5**, 418-434.
- Miller, M.J., T.N. Palmer, and R. Swinbank, 1989: Parameterization and influence of subgrid scale orography in general circulation and numerical weather prediction models. *Meteor. Atmos. Phys.*, **40**, 84-109.
- Mlawer, E.J., S.J. Taubman, P.D. Brown, M.J. Iacono, and S.A. Clough, 1997: Radiative transfer for inhomogeneous atmospheres: RRTM, a validated k-correlated model for the longwave. *J. Geophys. Res.*, **102**, 16663-16682.
- Nordeng, T.E., 1994: Extended versions of the convective parameterization scheme at ECMWF and their impact on the mean and transient activity of the model in the

- tropics. Technical Memorandum No. 206, European Centre for Medium-Range Weather Forecasts, Reading, United Kingdom.
- Palmer, T.N., G.J. Shutts, and R. Swinback, 1986: Alleviation of a systematic westerly bias in general circulation and weather prediction models through an orographic wave drag parameterization. *Q. J. Roy. Meteor. Soc.*, **112**, 1001-1031.
- Phillips, T.J., L.C. Corsetti, and S.L. Grotch, 1995: The impact of horizontal resolution on moist processes in the ECMWF model. *Clim. Dyn.*, **11**, 85-102.
- Pope, V.D., J.A. Pamment, D.R. Jackson, and A. Slingo, 2001: The representation of water vapour and its dependence on vertical resolution in the Hadley Centre climate model. *J. Climate*, **14**, 3065-3085.
- Pope, V.D. and R.A. Stratton, 2002: The processes governing horizontal resolution sensitivity in a climate model. *Clim. Dyn.*, **19**, 211-236.
- Rockel, B., E. Raschke, and B. Weyres, 1991: A parameterization of broad band radiative transfer properties of water, ice and mixed clouds. *Beitr. Phys. Atmos.*, **64**, 1-12.
- Roeckner, E., K. Arpe, L. Bengtsson, S. Brinkop, L. Dümenil, M. Esch, E. Kirk, F. Lunkeit, M. Ponater, B. Rockel, R. Sausen, U. Schlese, S. Schubert, and M. Windelband, 1992: Simulation of the present-day climate with the ECHAM model: Impact of model physics and resolution. Rep. No. **93**, Max-Planck-Institut für Meteorologie, Hamburg, Germany, 171 pp.
- Roeckner, E., K. Arpe, L. Bengtsson, M. Christoph, M. Claussen, L. Dümenil, M. Esch, M. Giorgetta, U. Schlese and U. Schulzweida, 1996: The atmospheric general circulation model ECHAM-4: Model description and simulation of present-day climate. Rep. No. **218**, Max Planck Institut für Meteorologie, Hamburg, 90 pp.
- Roeckner, E., G. Bäuml, L. Bonaventura, R. Brokopf, M. Esch, M. Giorgetta, S. Hagemann, I. Kirchner, L. Kornblüeh, E. Manzini, A. Rhodin, U. Schlese, U. Schulzweida, and A. Tompkins, 2003: The atmospheric general circulation model ECHAM5. Part I: Model description. Rep. No. **349**, Max-Planck-Institut für Meteorologie, Hamburg, Germany 127pp.
- Roesch, A., M. Wild, H. Gilgen, and A. Ohmura, 2001: A new snow cover fraction parameterization for the ECHAM4 GCM. *Clim. Dyn.*, **17**, 933-946.
- Schulz, J.-P., L. Dümenil, and J. Polcher, 2001: On the land surface-atmosphere coupling and its impact in a single-column atmosphere model. *J. Appl. Meteorol.*, **40**, 642-663.
- Simmons, A.J. and D.M. Burridge, 1981: An energy and angular-momentum conserving vertical finite difference scheme and hybrid vertical coordinates. *Mon. Wea. Rev.*, **109**, 758-766.
- Sperber, K.R., S. Hameed, G.L. Potter, and J.S. Boyle, 1994: Simulation of the northern summer monsoon in the ECMWF model: sensitivity to horizontal resolution. *Mon. Wea. Rev.*, **122**, 2461-2481.
- Stendel, M. and E. Roeckner, 1998: Impacts of horizontal resolution on simulated climate statistics in ECHAM4. Report No. 253, Max-Planck-Institut für Meteorologie, Hamburg, Germany, 57 pp.

- Stephenson, D.B., F. Chauvin, and J.F. Royer, 1998: Simulation of the Asian summer monsoon and its dependence on model horizontal resolution. *J. Meteor. Soc. Japan*, **76**, 237-265.
- Stratton, R.A., 1999: A high resolution AMIP integration using the Hadley Centre model HadAM2b. *Clim. Dyn.*, **15**, 9-28.
- Tanré, D., J.-F. Geleyn, and J.M. Slingo, 1984: First results of the introduction of an advanced aerosol-radiation interaction in the ECMWF low resolution global model. In: H. Gerber and A. Deepak (Eds.) *Aerosols and their Climatic Effects*, pp. 133-177. A. Deepak, Hampton, Virginia, USA.
- Tiedtke, M., 1989: A comprehensive mass flux scheme for cumulus parameterization in large-scale models. *Mon. Wea. Rev.*, **117**, 1779-1800.
- Tiedtke, M., 1993: Representation of clouds in large-scale models. *Mon. Wea. Rev.*, **121**, 3040-3061.
- Tompkins, A.M., 2002: A prognostic parameterization for the subgrid-scale variability of water vapor and clouds in large-scale models and its use to diagnose cloud cover. *J. Atmos. Sci.*, **59**, 1917-1942.
- Tompkins, A.M. and K.A. Emanuel, 2000: The vertical resolution sensitivity of simulated equilibrium temperature and water vapour profiles. *Q. J. Roy. Meteor. Soc.*, **126**, 1219-1238.
- Williamson, D.L., 1999: Convergence of atmospheric simulations with increasing horizontal resolution and fixed forcing scales. *Tellus*, **51A**, 663-673.
- Williamson, D.L. and J.G. Olsen, 1998: A comparison of semi-Lagrangian and Eulerian polar climate simulations. *Mon. Wea. Rev.*, **126**, 991-1000.
- Williamson, D.L., J.T. Kiehl, and J.J. Hack, 1995: Climate sensitivity of the NCAR community climate model (CCM2) to horizontal resolution. *Clim. Dyn.*, **11**, 377-397.

Resolution	Grid (deg)	Δt (min)	ASR (clear)	OLR (clear)	SW (cloud)	LW (cloud)	ASR (all)	OLR (all)	ASR-OLR (all)
T21 L19	5.62	40	286.8	258.8	- 53.6	27.0	233.1	231.8	1.3
T31 L19	3.75	40	286.6	259.1	- 53.8	27.3	233.8	231.9	1.9
T42 L19	2.81	30	286.7	259.6	- 53.0	27.2	233.7	232.4	1.3
T63 L19	1.87	20	286.7	260.1	- 53.3	27.2	233.4	232.9	0.5
T85 L19	1.41	15	286.8	260.2	- 53.6	27.4	233.2	232.8	0.4
T106 L19	1.12	12	286.8	260.2	- 53.7	27.3	233.1	232.9	0.3
T42 L31	2.81	20	286.7	260.5	- 53.2	28.3	233.5	232.2	1.3
T63 L31	1.87	12	286.8	261.3	- 53.0	28.3	233.7	233.1	0.6
T85 L31	1.41	8	286.8	261.8	- 52.8	27.8	234.0	234.0	0.0
T106 L31	1.12	6	286.8	262.2	- 51.5	27.1	235.3	235.1	0.2
T159 L31	0.75	4	286.7	262.4	- 50.6	25.9	236.2	236.5	- 0.3
Observed			288	264	- 48	30	235*	235*	0.0*

Table 1: Model resolutions, time steps (Δt), and global annual mean top-of-atmosphere radiation budget. The radiation time step is 2h in each experiment. The simulated 15-year mean radiative fluxes (Wm^{-2}) are clear-sky and all-sky absorbed shortwave radiation (ASR), outgoing longwave (OLR), net radiation (ASR-OLR), and shortwave (SW) and longwave (LW) cloud-radiative forcing. Observational estimates for clear-sky fluxes and cloud-radiative forcing are from 2 years of Earth Radiation Budget experiment (ERBE) data (Hartmann, 1993).

* All-sky fluxes are taken from Kiehl and Trenberth (1997) who adjusted the ERBE SW fluxes to obtain a zero value in net radiation. Without this adjustment an imbalance of about 6 Wm^{-2} would occur that can be taken as the uncertainty in the global mean ERBE fluxes.

Variable	T200	T500	T850	Z200	Z500	Z850	SLP	U200	U500	U850
T21L19	6.20	2.00	1.89	8.10	6.46	5.05	6.31	7.77	4.82	3.40
T31L19	5.54	1.42	2.14	7.13	3.58	2.68	3.55	5.97	3.12	2.40
T42L19	5.12	1.00	2.02	7.04	3.25	1.93	2.55	4.48	2.37	1.92
T63L19	4.74	0.96	1.88	7.91	3.73	1.76	2.32	3.57	2.16	1.73
T85L19	4.64	1.14	1.80	8.80	4.13	1.78	2.32	3.64	2.26	1.71
T106L19	4.51	1.22	1.75	9.02	4.18	1.70	2.23	3.41	2.15	1.60
T42L31	5.10	1.15	1.81	6.33	2.63	2.13	2.81	5.60	2.57	1.92
T63L31	4.41	0.84	1.65	4.40	2.16	1.65	2.17	4.50	2.02	1.51
T85L31	4.11	0.78	1.57	3.69	2.07	1.48	1.95	3.92	1.91	1.38
T106L31	3.91	0.79	1.57	3.31	2.07	1.40	1.86	3.44	1.74	1.26
T159L31	3.22	0.80	1.59	2.91	1.98	1.30	1.75	2.84	1.64	1.13

Table 2: Root-mean-squared-errors (RMSE) with respect to ERA-15, averaged over all four seasons, for temperature (T), geopotential height (Z), and zonal wind (U) at pressure levels 200, 500 and 850 hPa, respectively, and for mean sea level pressure (SLP). The RMSE are given in units of °C for T, decameter for Z, hPa for mean sea level pressure (SLP), and m/s for U.

Bold: Increasing errors with increasing horizontal resolution.

	T200	T500	T850	Z200	Z500	Z850	SLP	U200	U500	U850
T42	1.00	1.15	0.90	0.90	0.81	1.10	1.10	1.25	1.08	1.00
T63	0.93	0.88	0.88	0.56	0.58	0.94	0.94	1.26	0.94	0.87
T85	0.89	0.68	0.87	0.42	0.50	0.83	0.84	1.08	0.85	0.81
T106	0.87	0.65	0.90	0.37	0.49	0.82	0.83	1.01	0.81	0.79

Table 3: Impact of vertical resolution on systematic errors. Shown is the ratio of seasonal mean RMSE (L31/L19) for different horizontal resolutions.

Bold: larger errors in L31 simulation than in L19 simulation.

Spectral resolution	Δx at 45° [km]	Δz (N_1) [m]	Δz (N_2) [m]	Δz (L19) at 500 hPa [m]	Δz (L31) at 500 hPa [m]
T21	442	2110	3377	1500	750
T31	295	1408	2254	1500	750
T42	221	1055	1688	1500	750
T63	147	702	1123	1500	750
T85	111	530	848	1500	750
T106	88	420	672	1500	750
T159	59	282	451	1500	750

Table 4: Vertical grid spacing (Δz) for L19 and L31 models compared to that derived from the Rossby ratio of horizontal and vertical scales, $\Delta x/\Delta z = (N/f_0)$, where f_0 is the characteristic Coriolis parameter and N is the Brunt-Väisälä frequency. In this example, f_0 (45°) = 10^{-4} s^{-1} , $N_1 = 2\pi/300 \text{ s}^{-1}$ and $N_2 = 2\pi/480 \text{ s}^{-1}$, respectively (Lindzen and Fox-Rabinowitz, 1989).

Bold: ‘consistency’ between horizontal and vertical resolution for quasi-geostrophic flow at 45° .

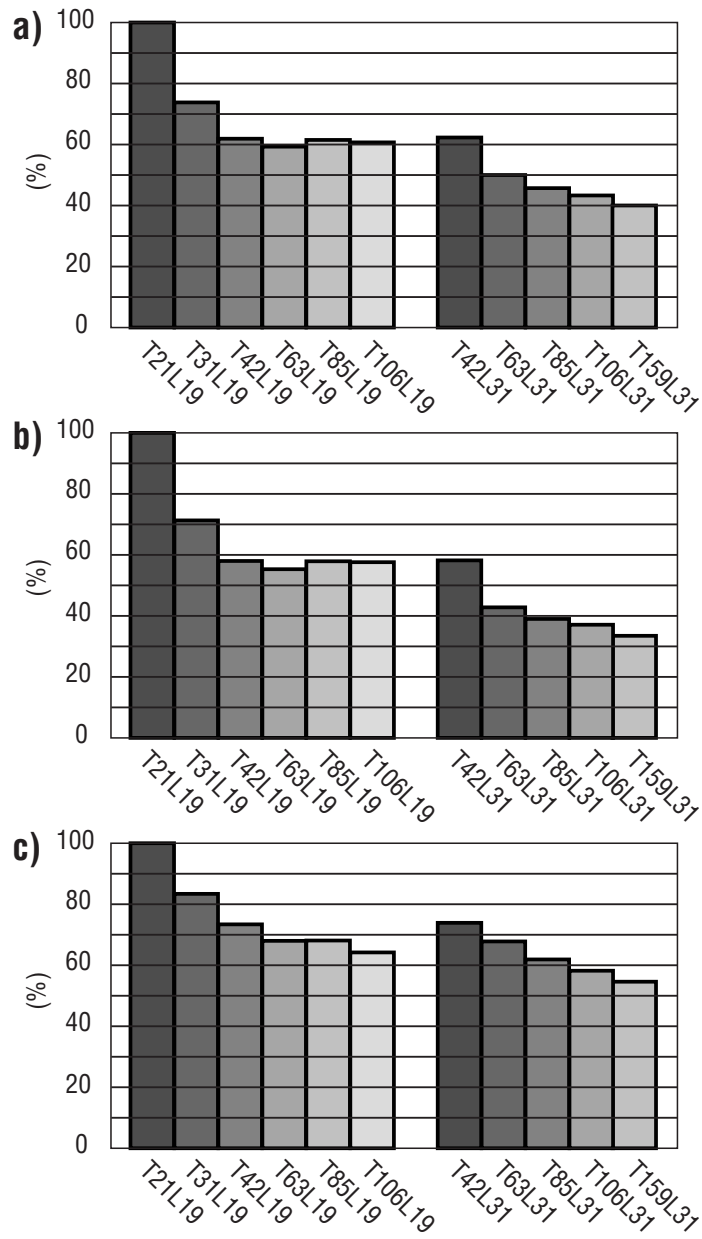


Figure 1: Resolution dependence of overall RMSE (see text) with respect to ERA-15. Shown are normalized RMSE of total fields (a), of zonal means (b), and of stationary waves (c), expressed as percentages of the respective T21L19 errors.

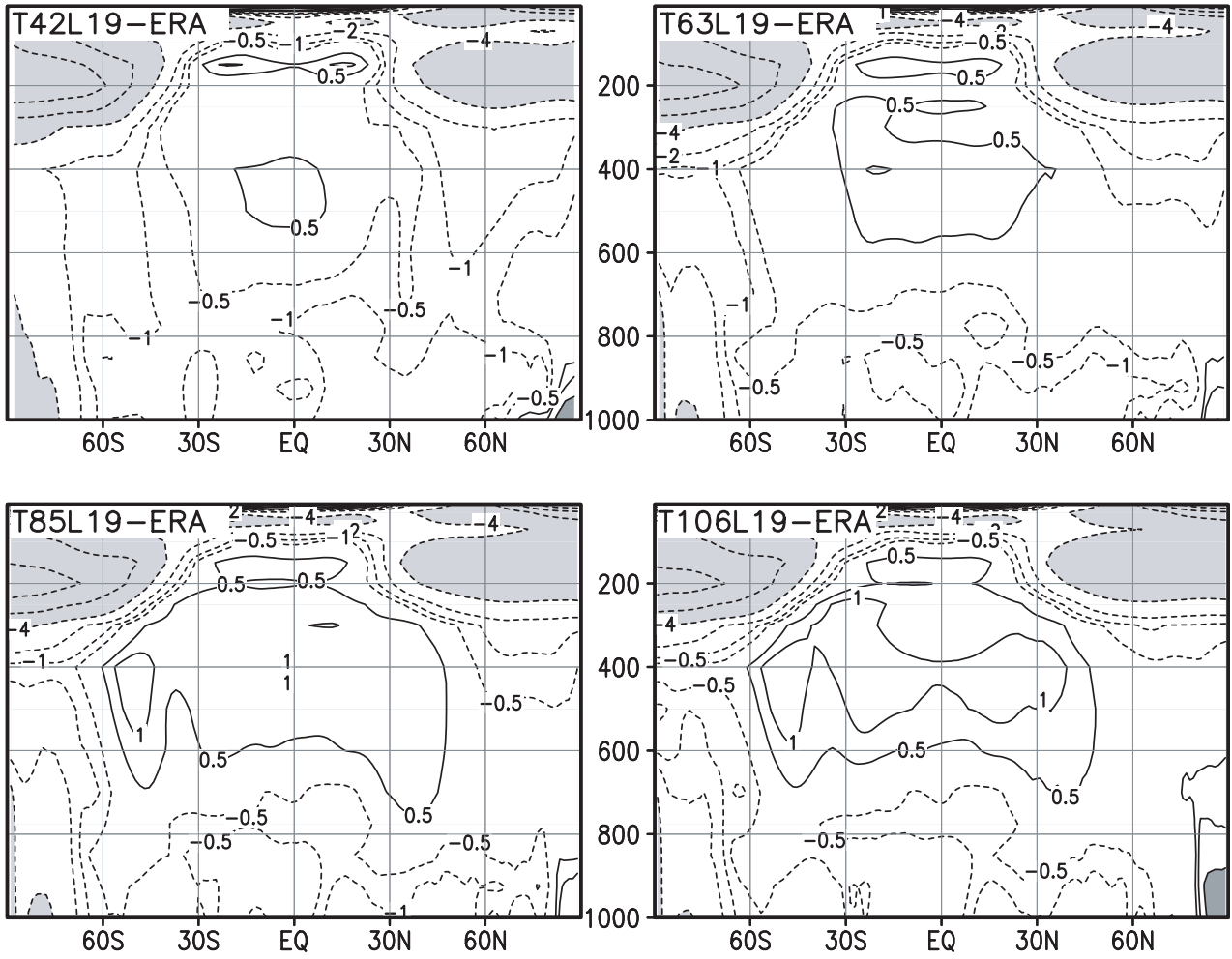


Figure 2: Latitude–height (pressure in hPa) distributions of zonal mean temperature errors (DJF) in L19 simulations. Contours are ± 0.5 1 2 4 8 12 $^\circ\text{C}$. Light shading for differences < -4 $^\circ\text{C}$. Dark shading for differences > 2 $^\circ\text{C}$.

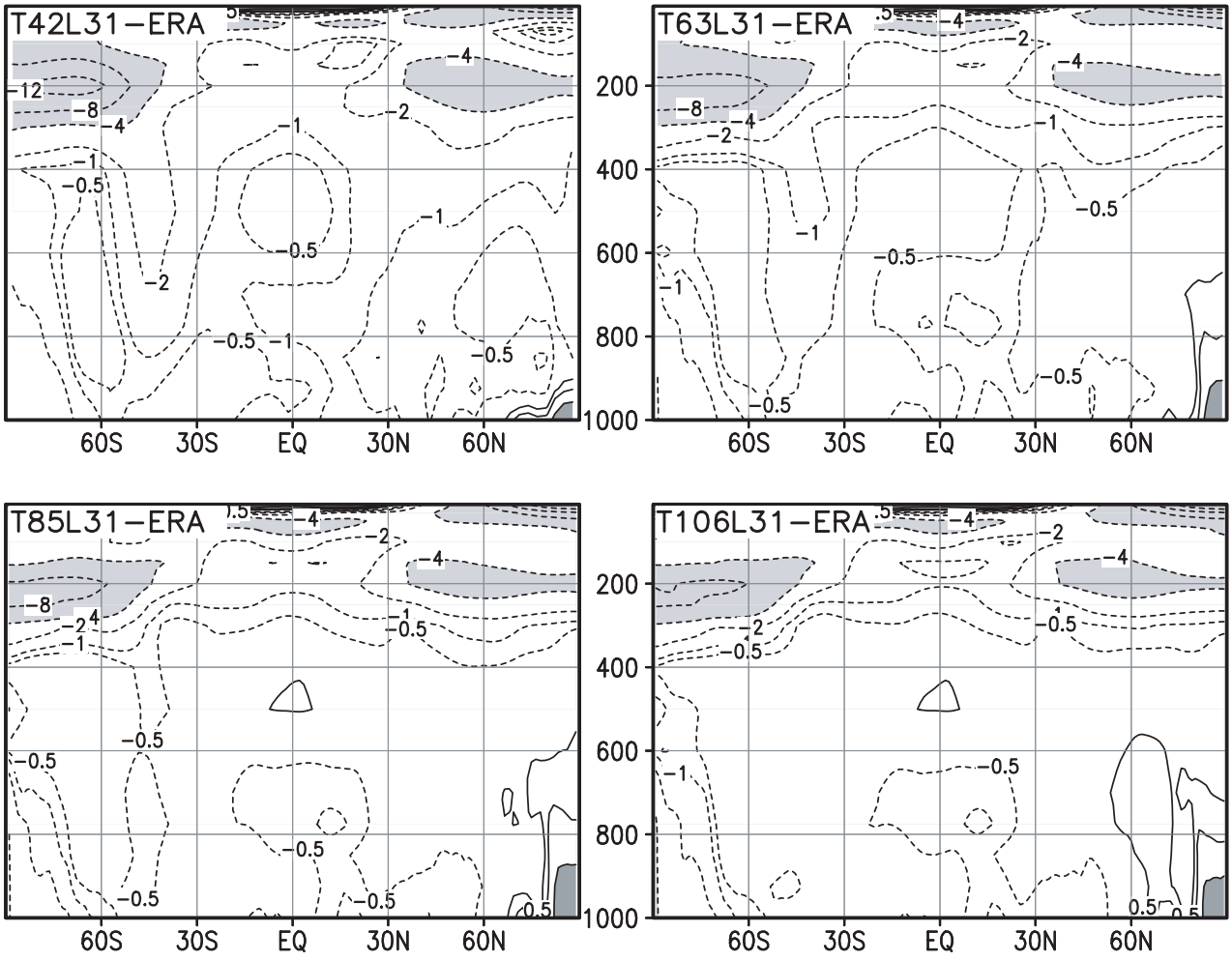


Figure 3: As Fig. 2 but for L31 simulations.

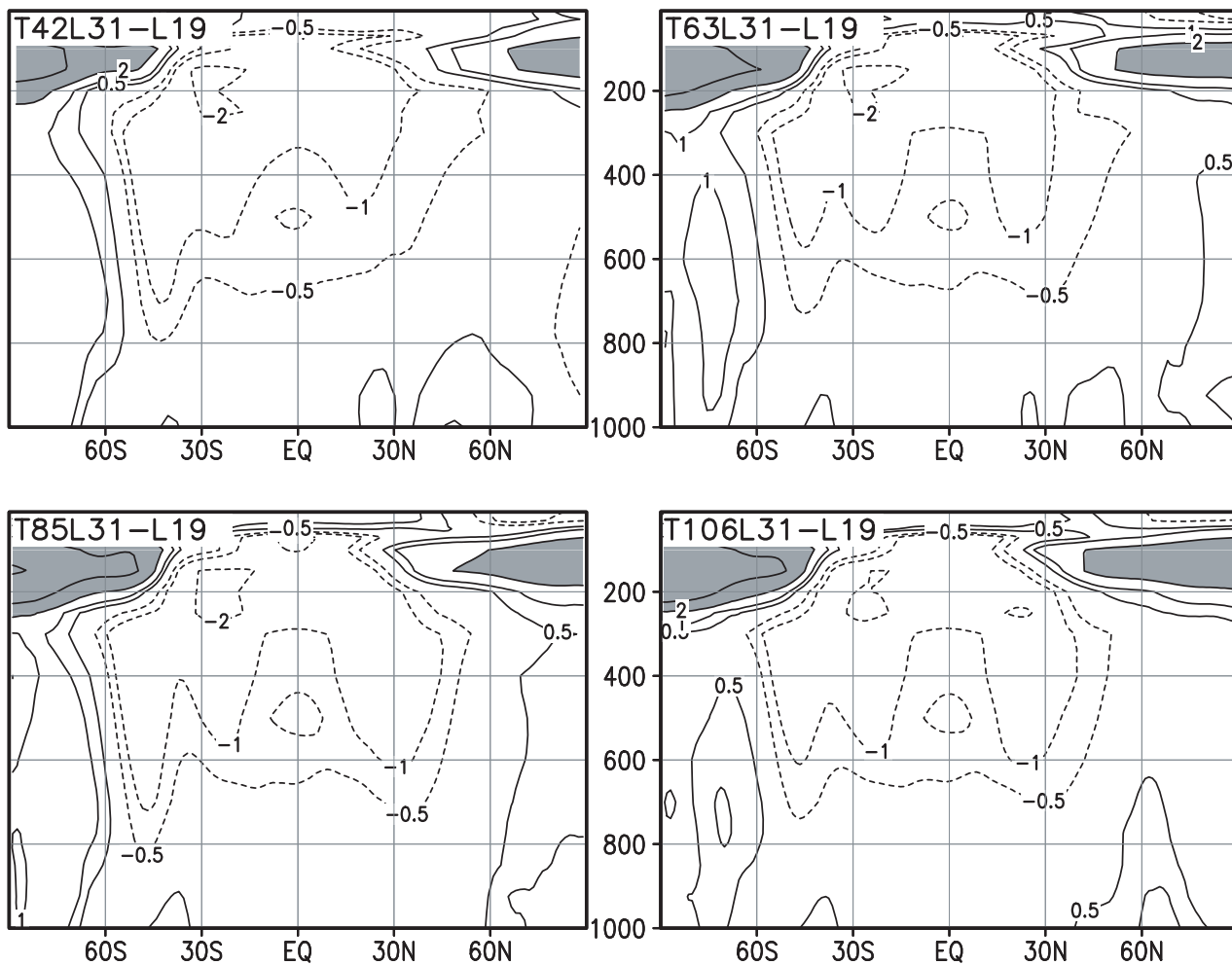


Figure 4: As Fig. 2 but for model differences L31-L19.

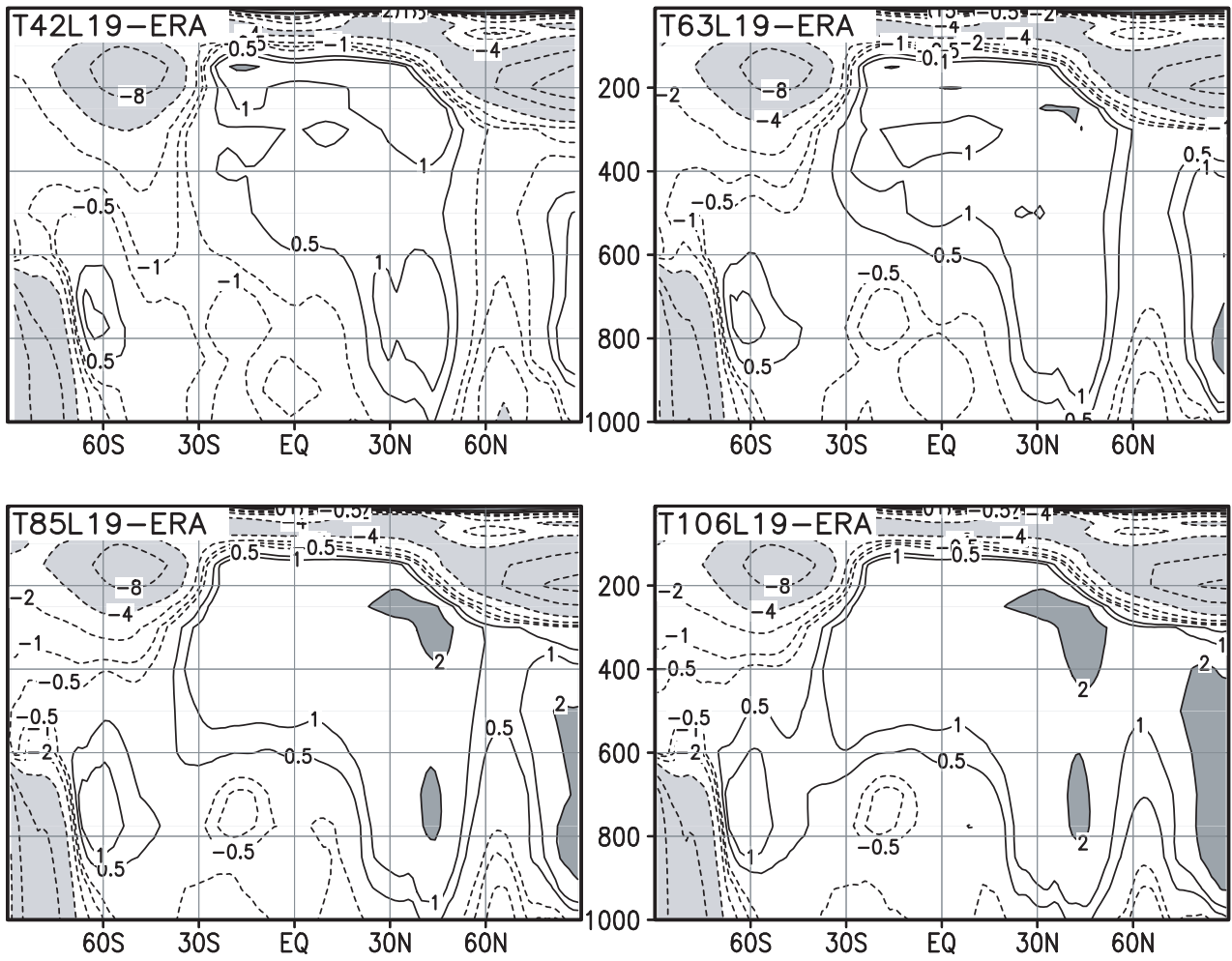


Figure 5: Latitude–height (pressure in hPa) distributions of zonal mean temperature errors (JJA) in L19 simulations. Contours are $\pm 0.5, 1, 2, 4, 8, 12\text{ }^\circ\text{C}$. Light shading for differences $< -4\text{ }^\circ\text{C}$. Dark shading for differences $> 2\text{ }^\circ\text{C}$.

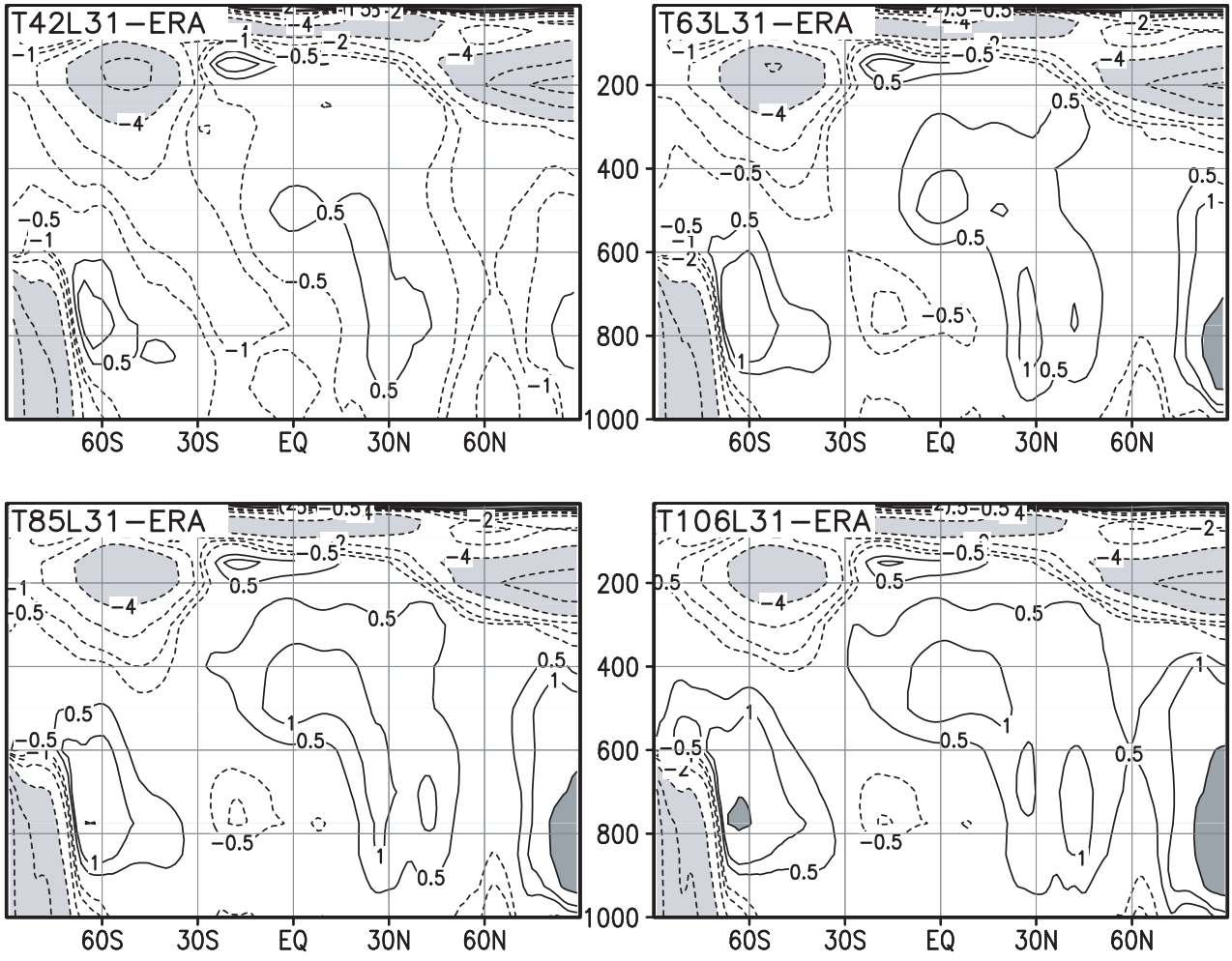


Figure 6: As Fig. 5 but for L31 simulations.

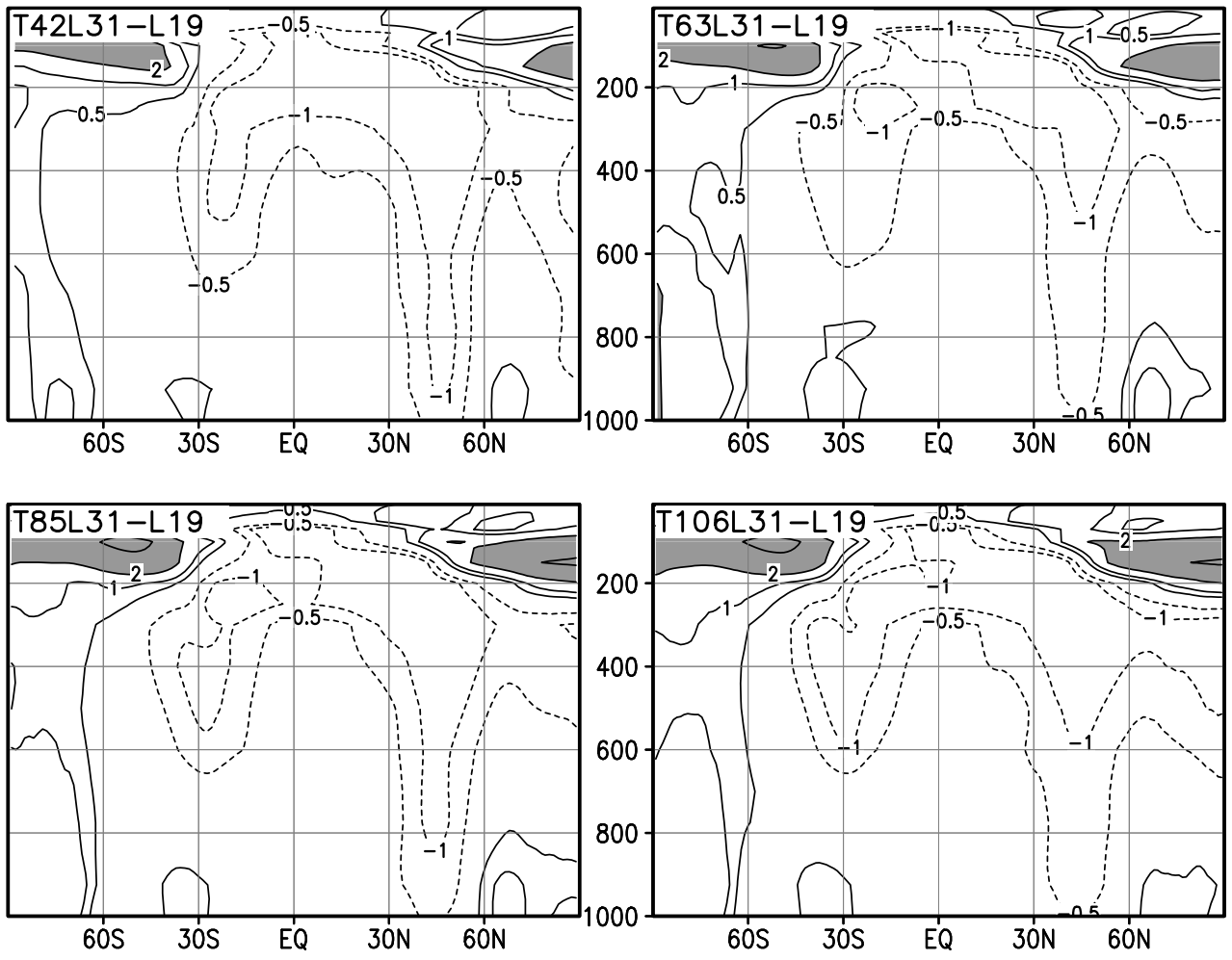
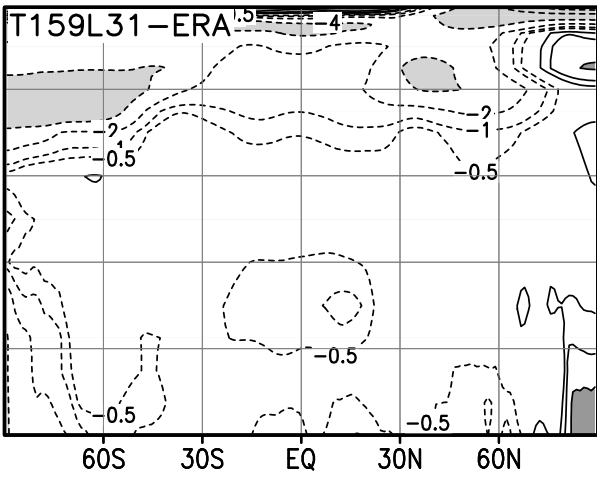


Figure 7: As Fig. 5 but for L31-L19.

DJF



JJA

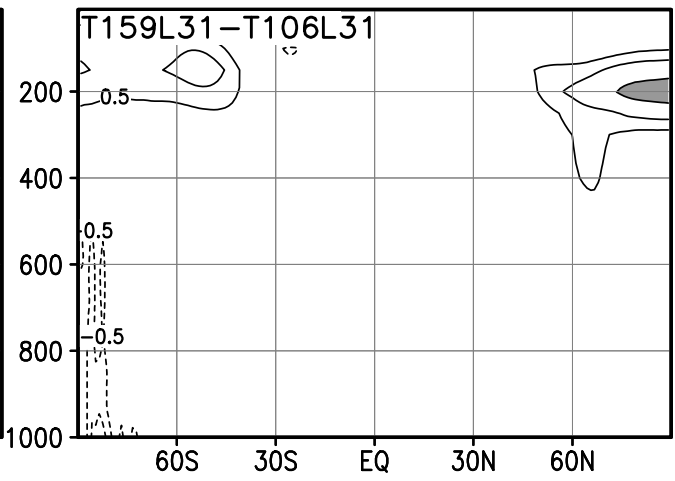
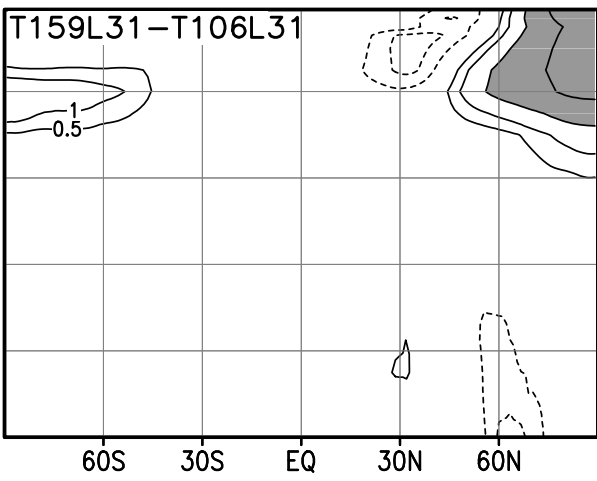
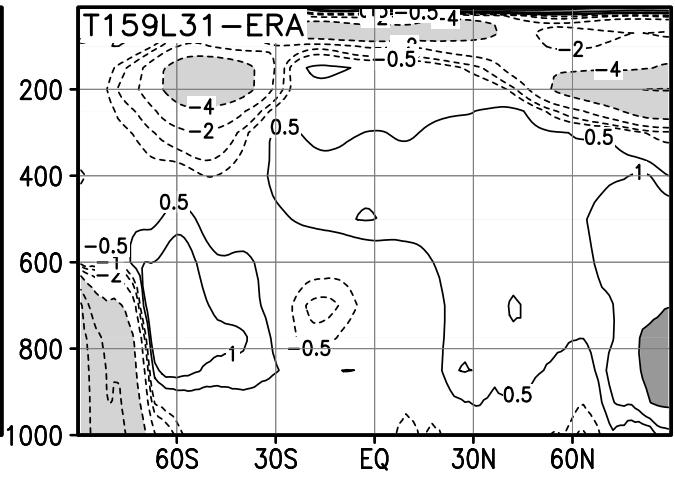


Figure 8: Latitude–height (pressure in hPa) distributions of DJF and JJA temperature errors in the T159L31 simulation (top panels) and model differences T159L31–T106L31 (bottom panels). Contours are $\pm 0.5, 1, 2, 4, 8, 12$ °C. Light shading for differences < -4 °C. Dark shading for differences > 2 °C.

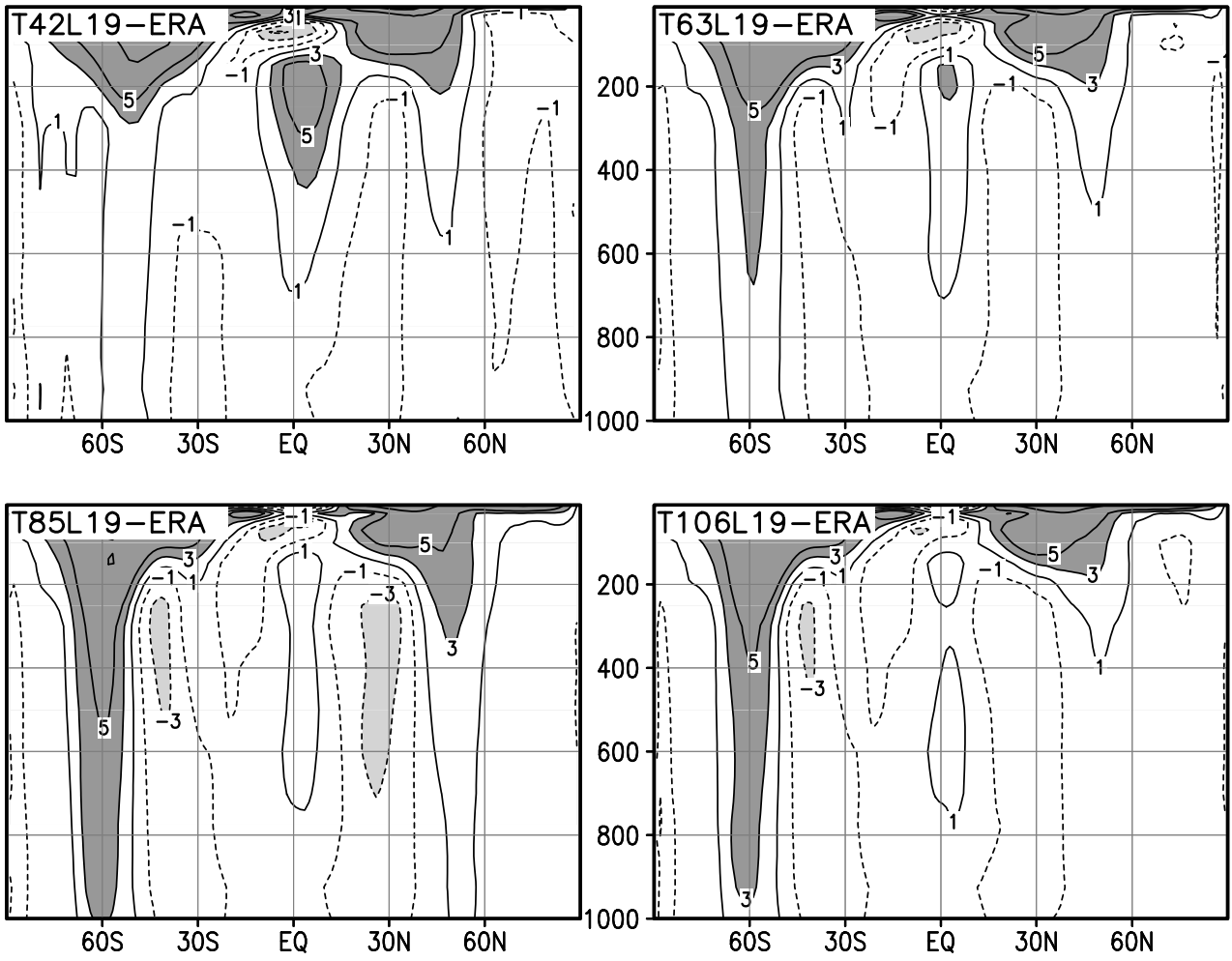


Figure 9: Latitude–height (pressure in hPa) distributions of zonal mean zonal wind errors (DJF) in L19 simulations. Contours are $\pm 1, 3, 5, 10$ m/s. Light shading for differences < -3 m/s. Dark shading for differences > 3 m/s.

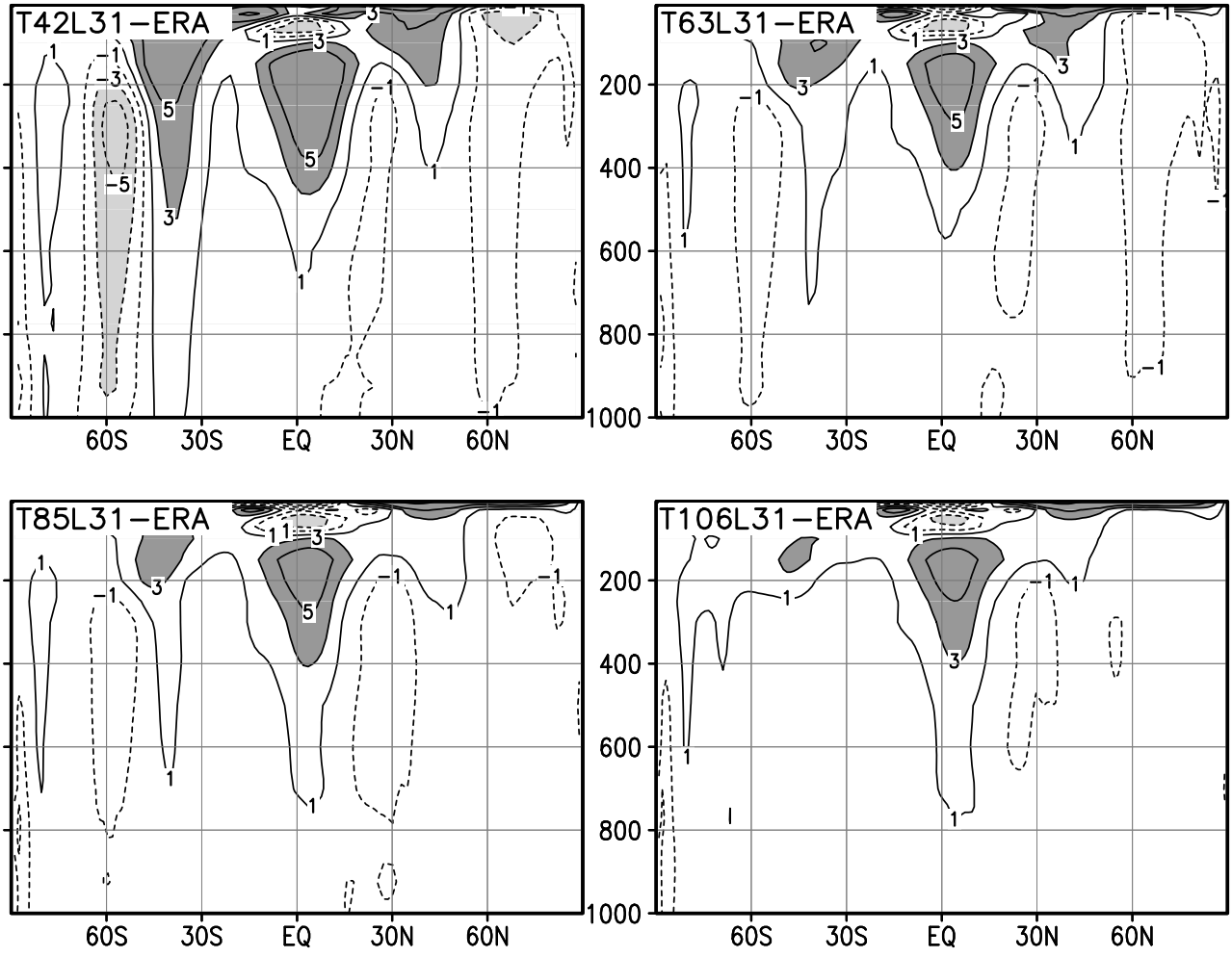


Figure 10: As Fig. 9 but for L31 simulations.

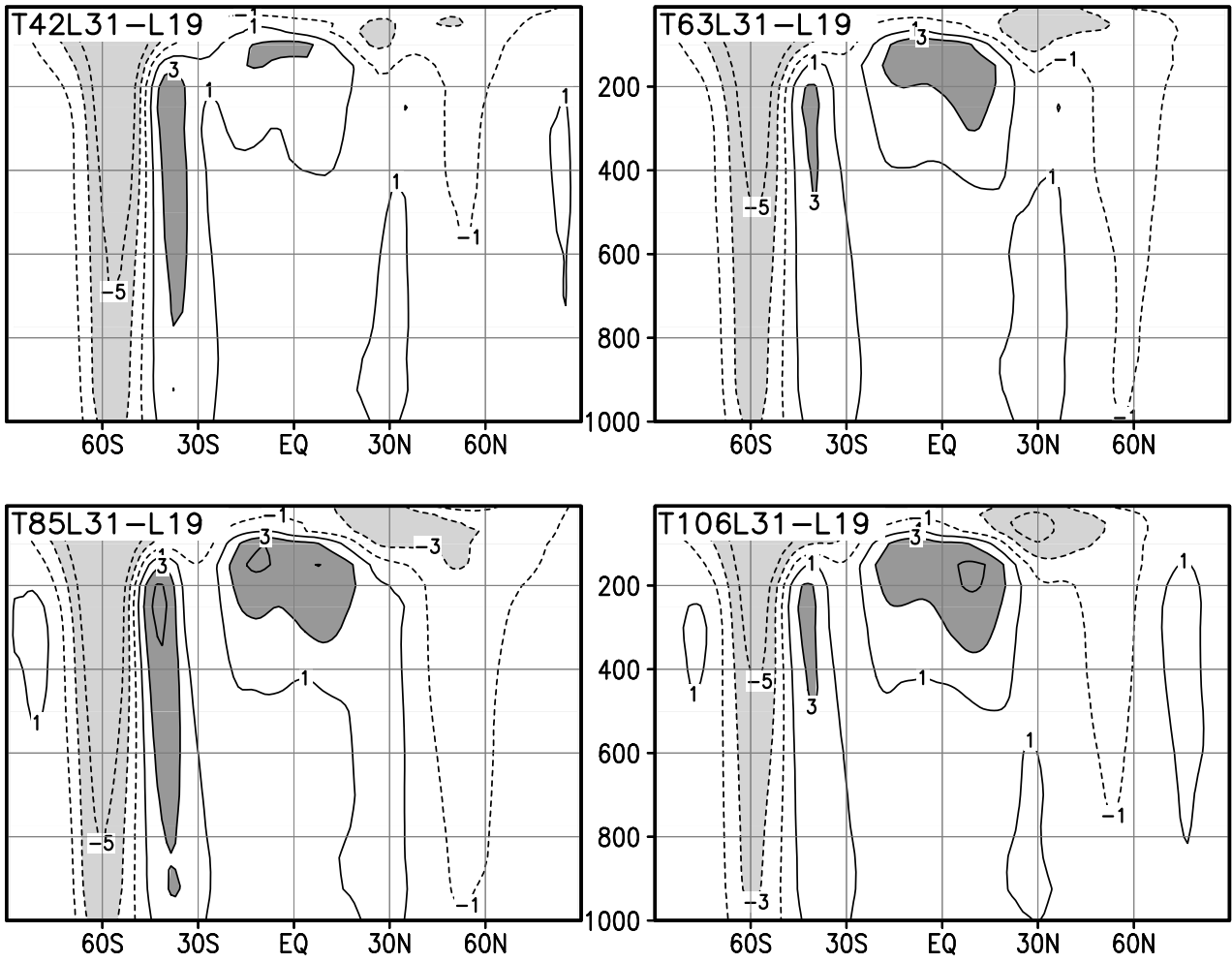


Figure 11: As Fig. 9 but for differences L31-L19.

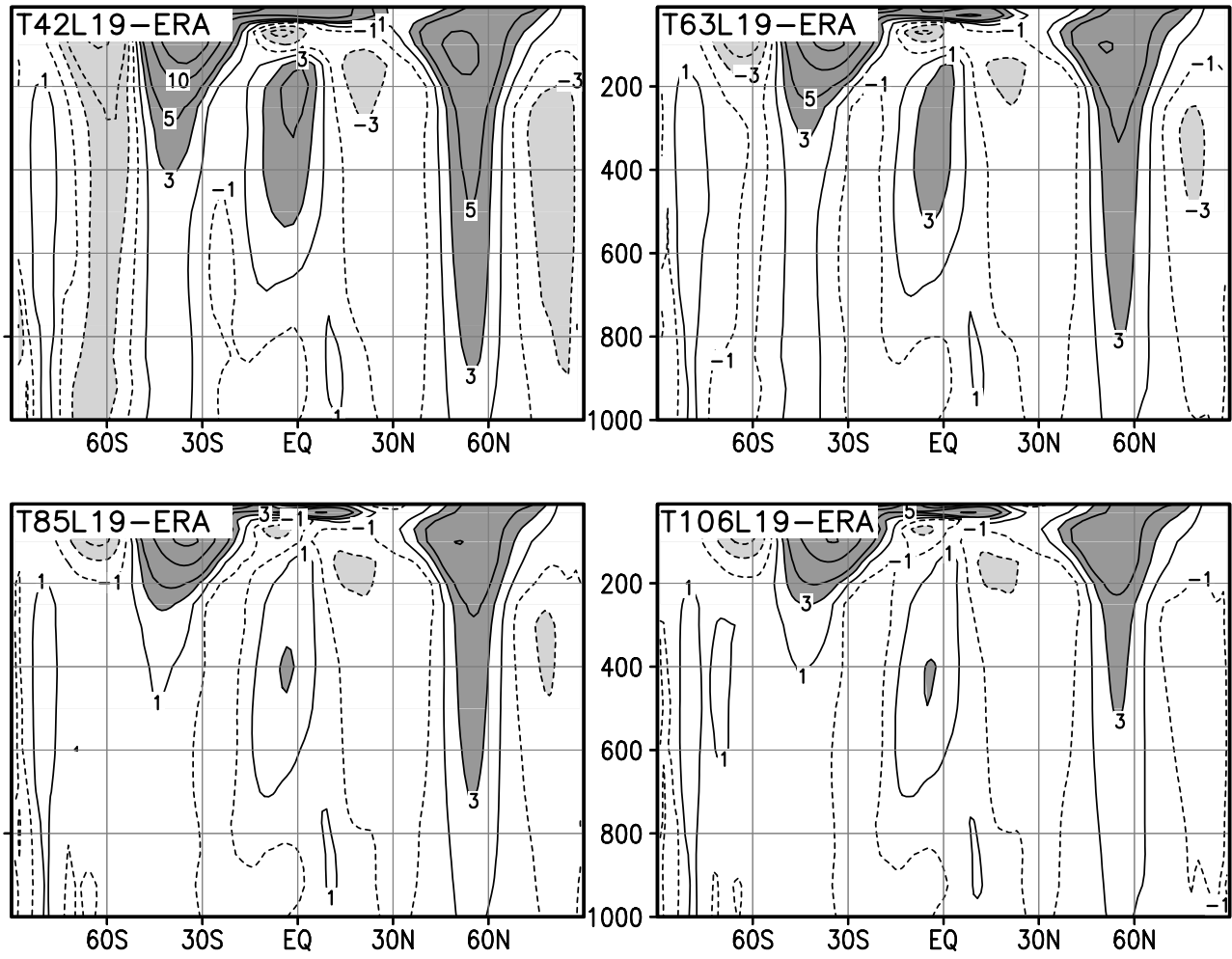


Figure 12: Latitude–height (pressure in hPa) distributions of zonal mean zonal wind errors (JJA) in L19 simulations. Contours are $\pm 1, 3, 5, 10$ m/s. Light shading for differences < -3 m/s. Dark shading for differences > 3 m/s.

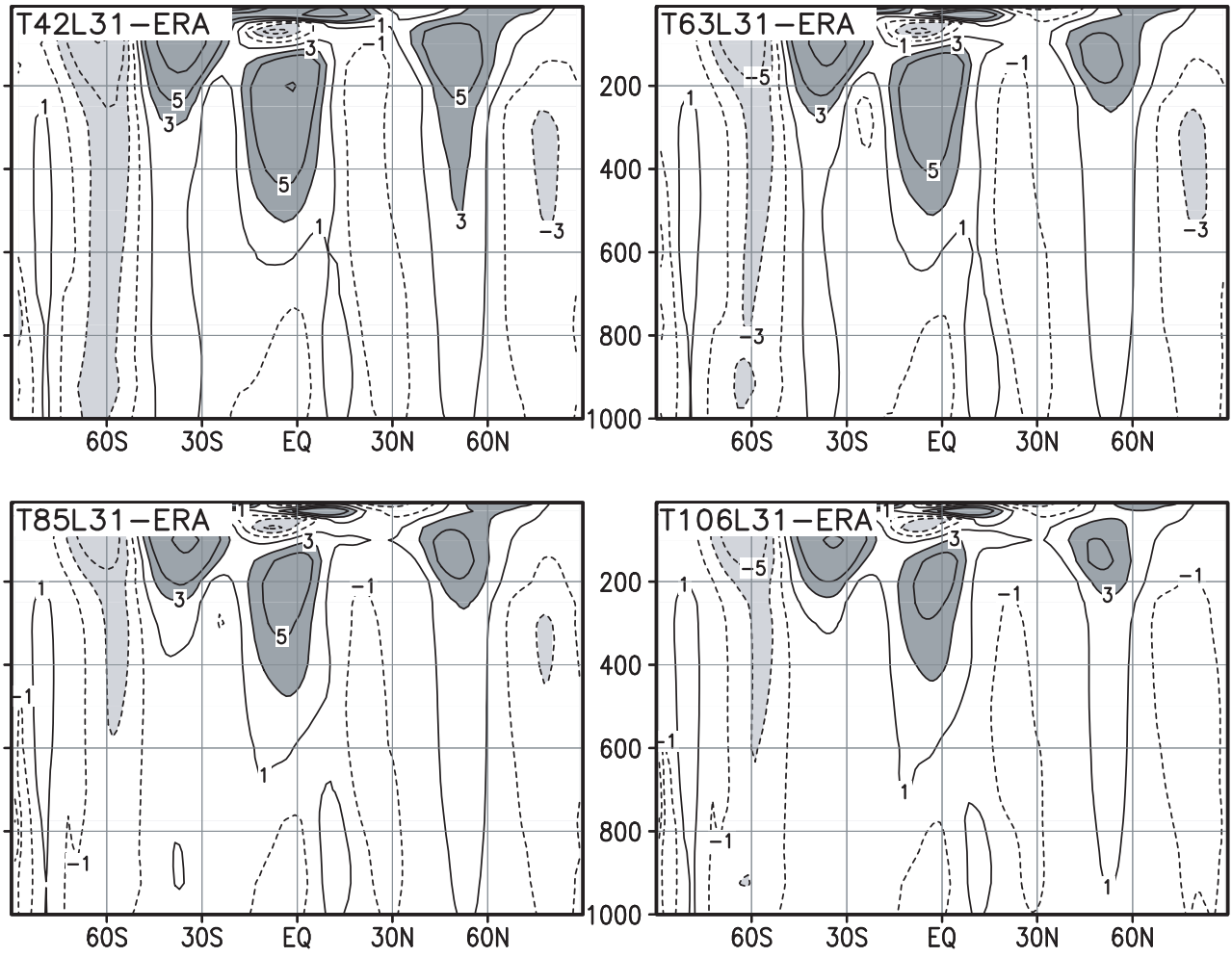


Figure 13: As Fig. 12 but for L31 simulations.

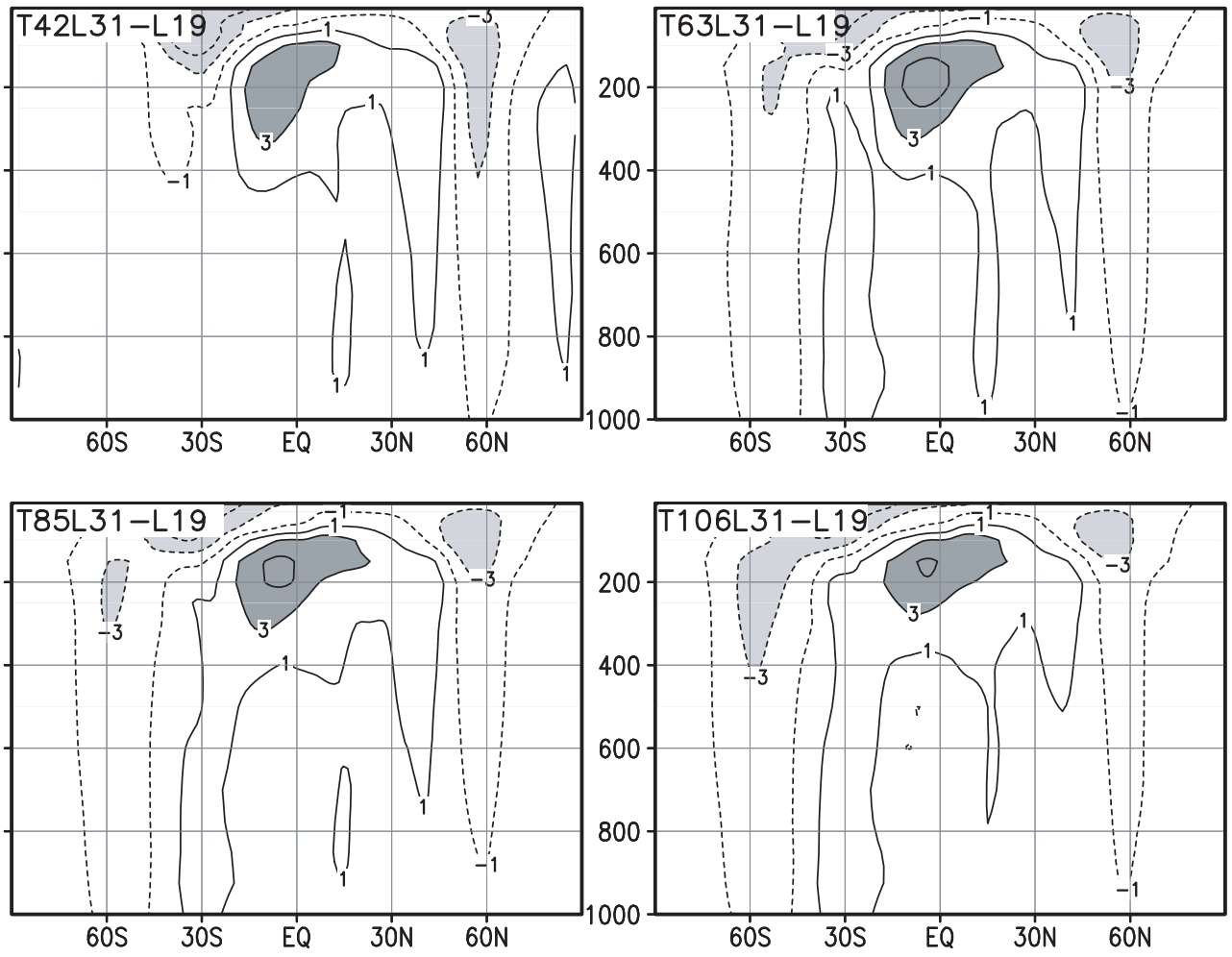


Figure 14: As Fig. 12 but for differences L31-L19.

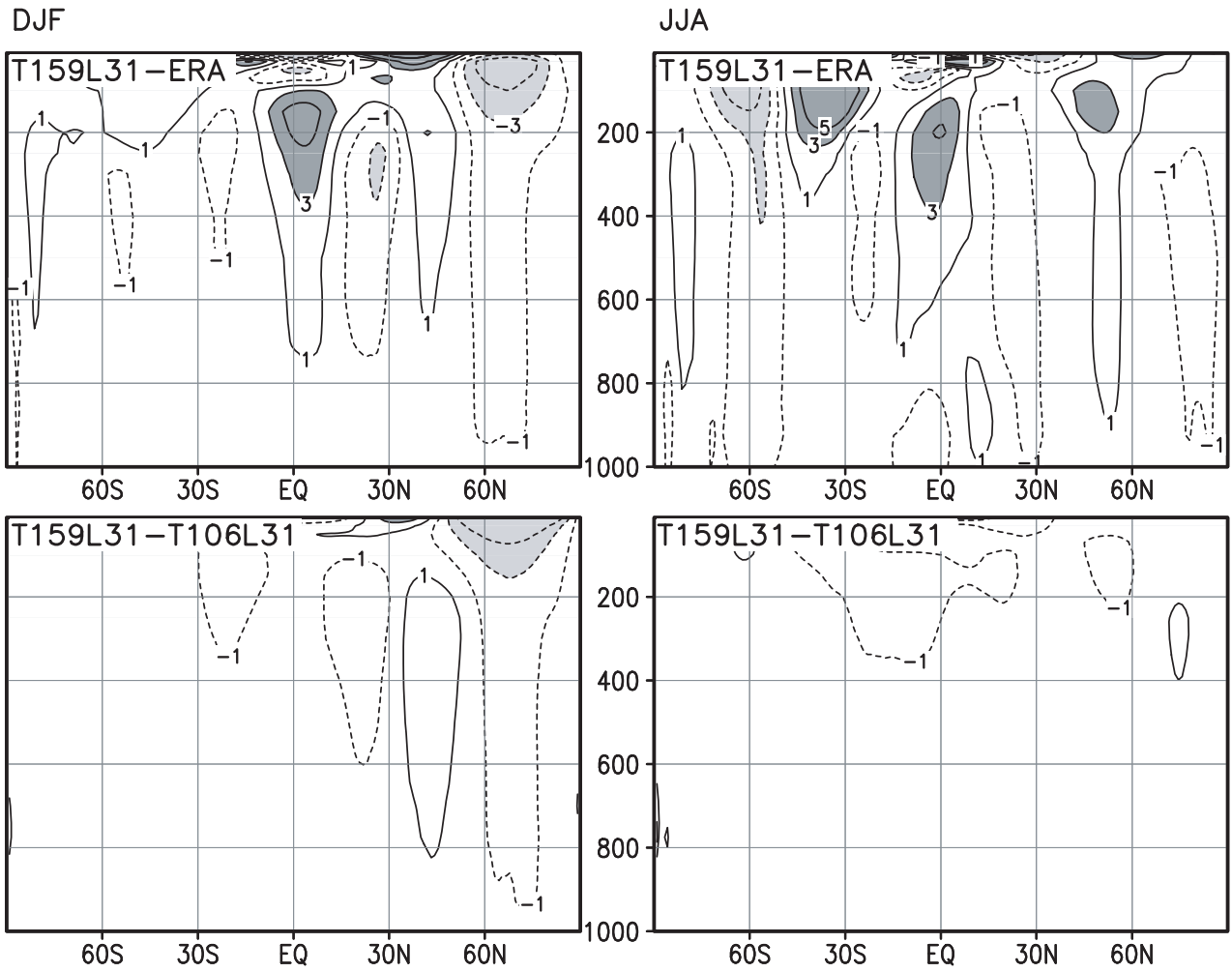


Figure 15: Latitude–height (pressure in hPa) distributions of DJF and JJA zonal wind errors in the T159L31 simulation (top panels) and model differences T159L31–T106L31 (bottom panels). Contours are $\pm 1, 3, 5, 10$ m/s. Light shading for differences < -3 m/s. Dark shading for differences > 3 m/s.

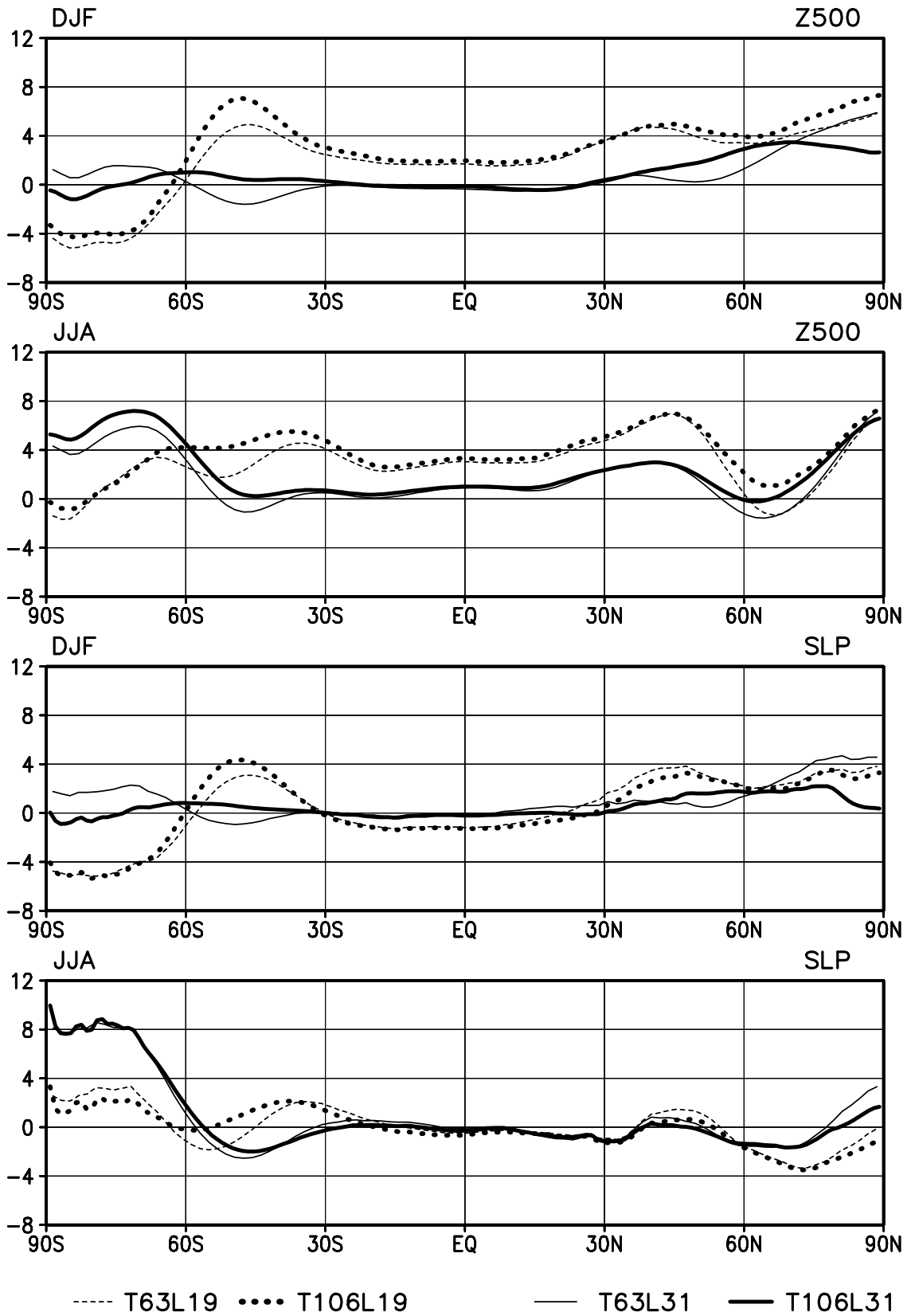


Figure 16: Errors in zonal mean 500 hPa geopotential height (Z500 in decameter) and zonal mean sea level pressure (SLP in hPa).

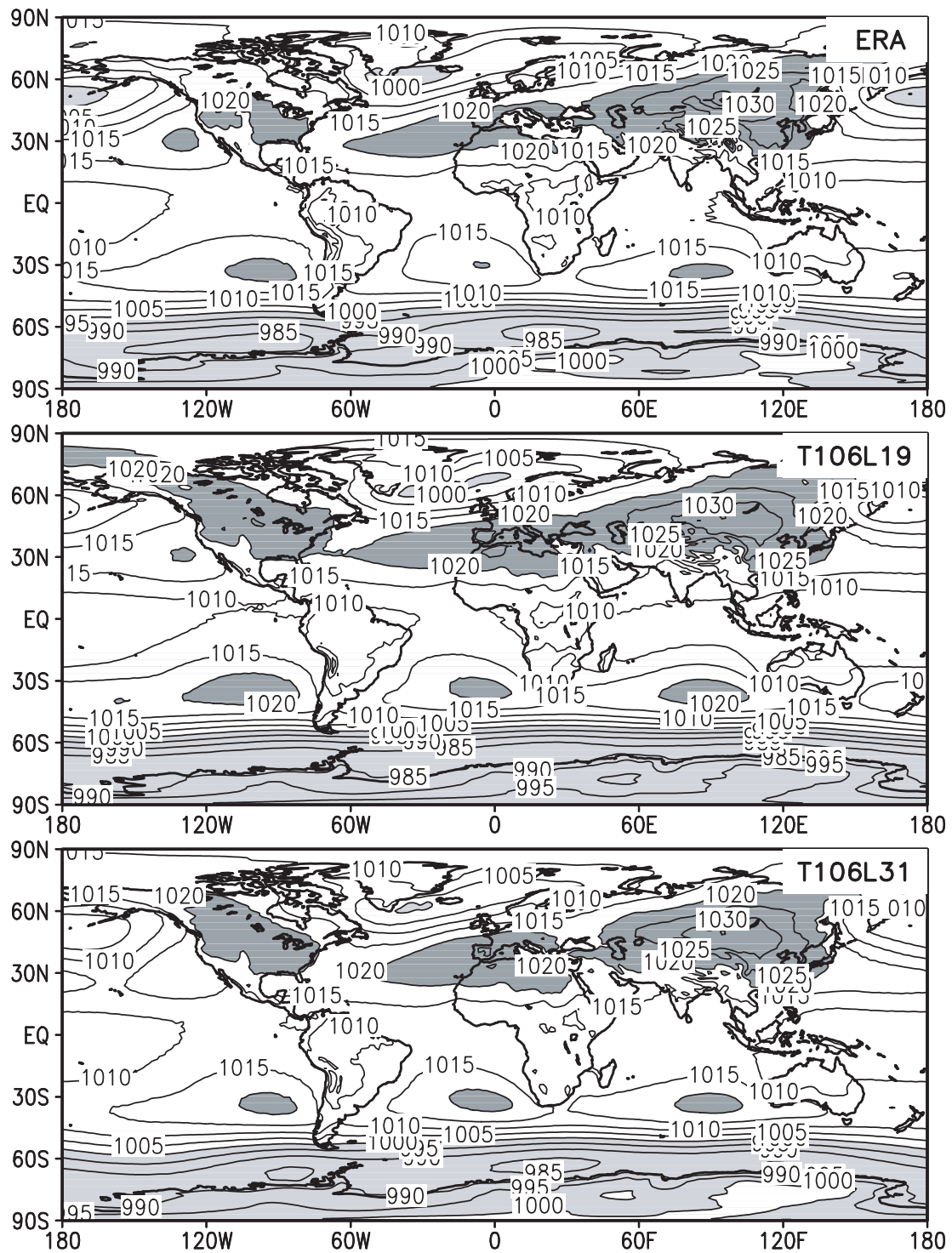


Figure 17: Comparison of observed (ERA-15) and model simulated geographic distributions of DJF sea level pressure. Contours every 5 hPa. Light shading for low pressure (< 1000 hPa), dark shading for high pressure (> 1020 hPa).

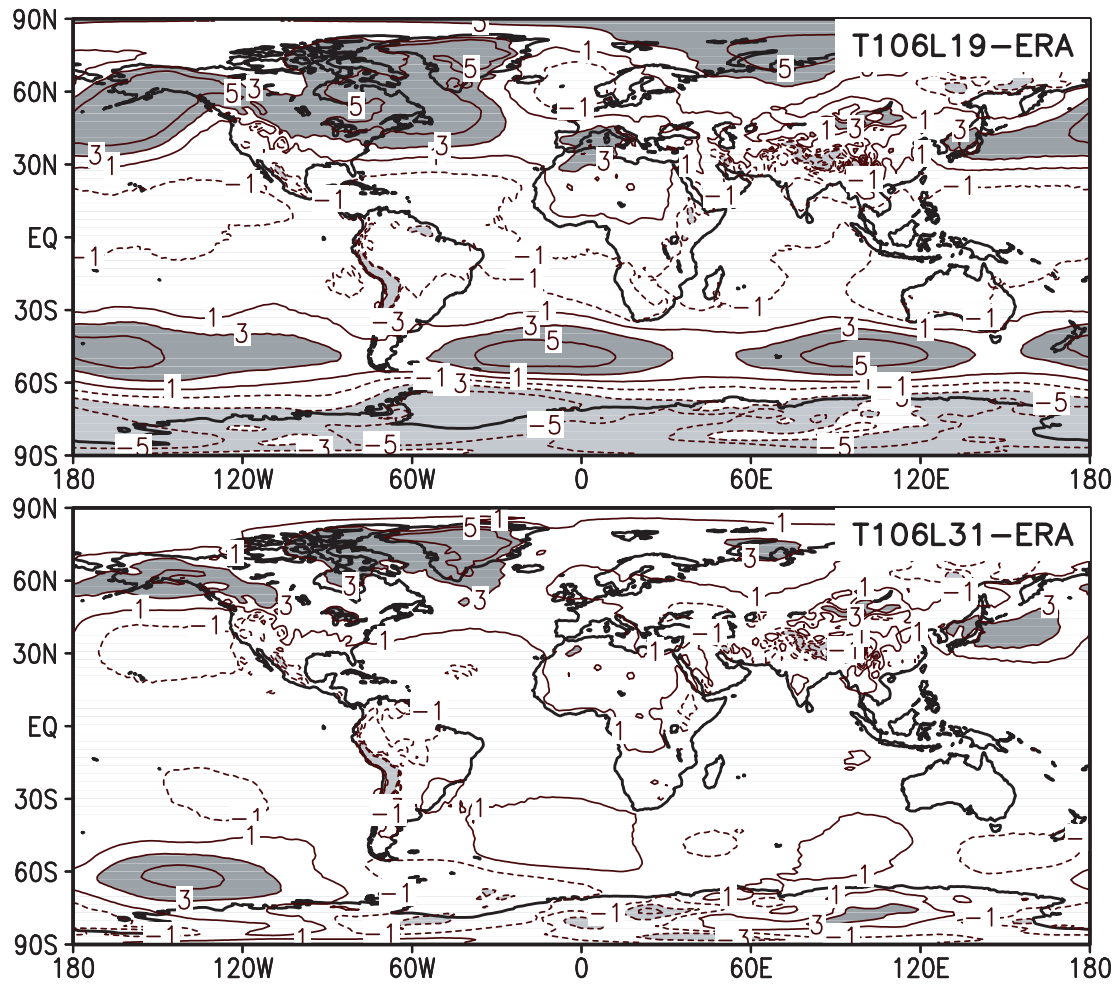


Figure 18: As Fig. 17 but for differences between model simulations and ERA-15. Contours are $\pm 1, 3, 5, 10$ hPa. Light shading for low-pressure biases in the simulations (< 3 hPa), dark shading for high-pressure biases (> 3 hPa).

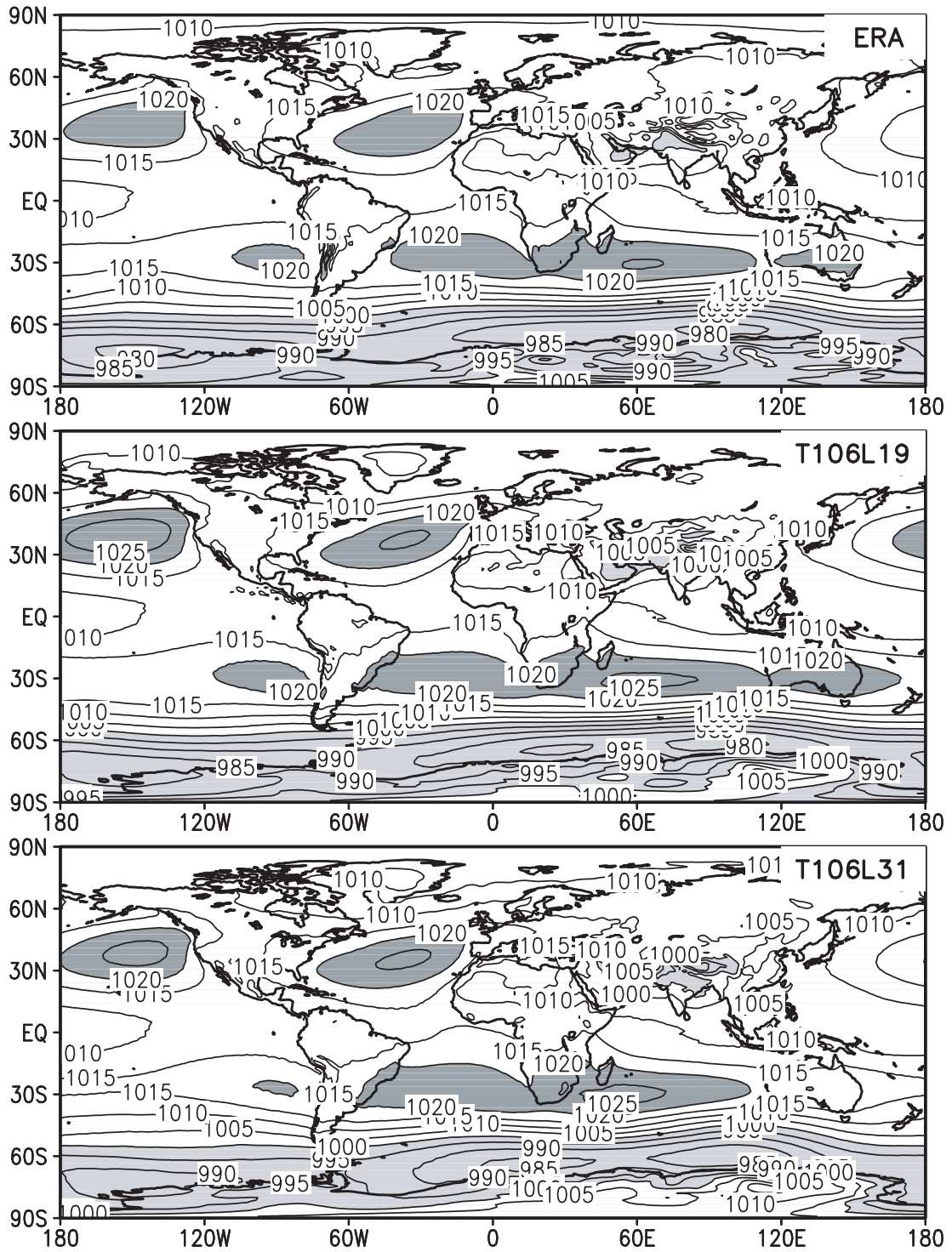


Figure 19: As Fig. 17 but for JJA.

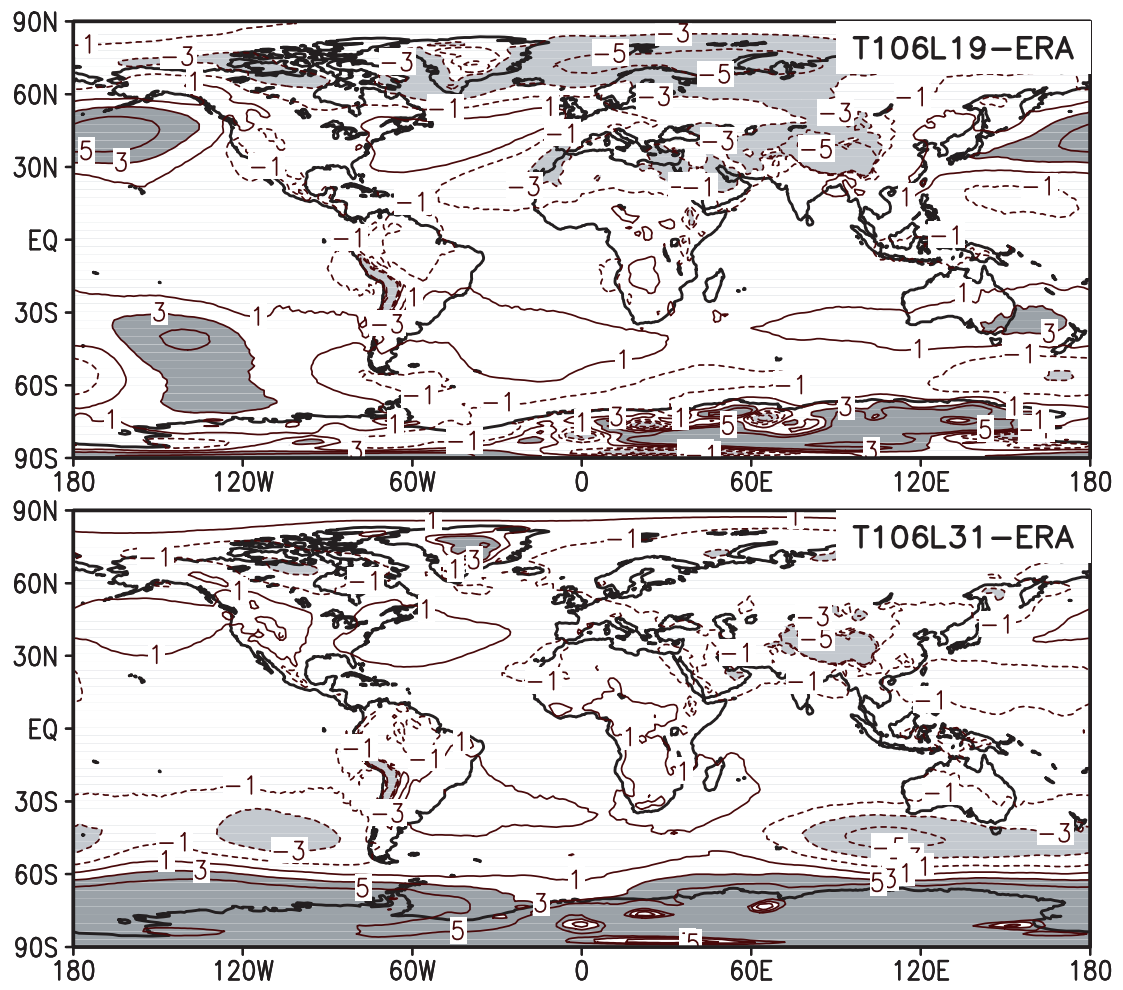


Figure 20: As Fig. 18 but for JJA.

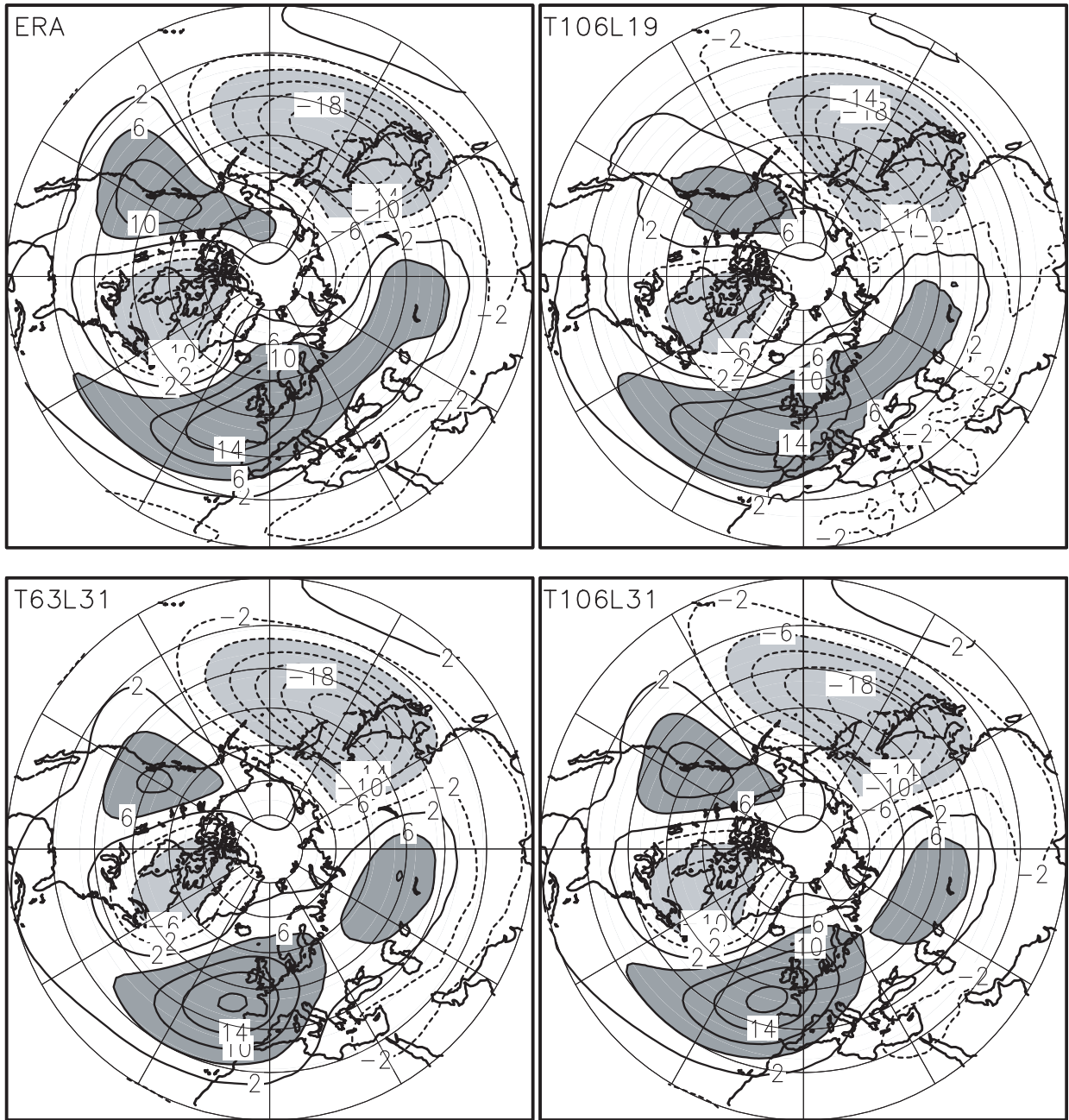


Figure 21: Comparison of observed (ERA-15) and model simulated DJF stationary wave patterns of 500 hPa geopotential height in the northern hemisphere. Contours are $\pm 2, 6, 10, 14, 18, 22$ decameter. Light shading for height anomalies < -6 decameter, dark shading for height anomalies > 6 decameter.

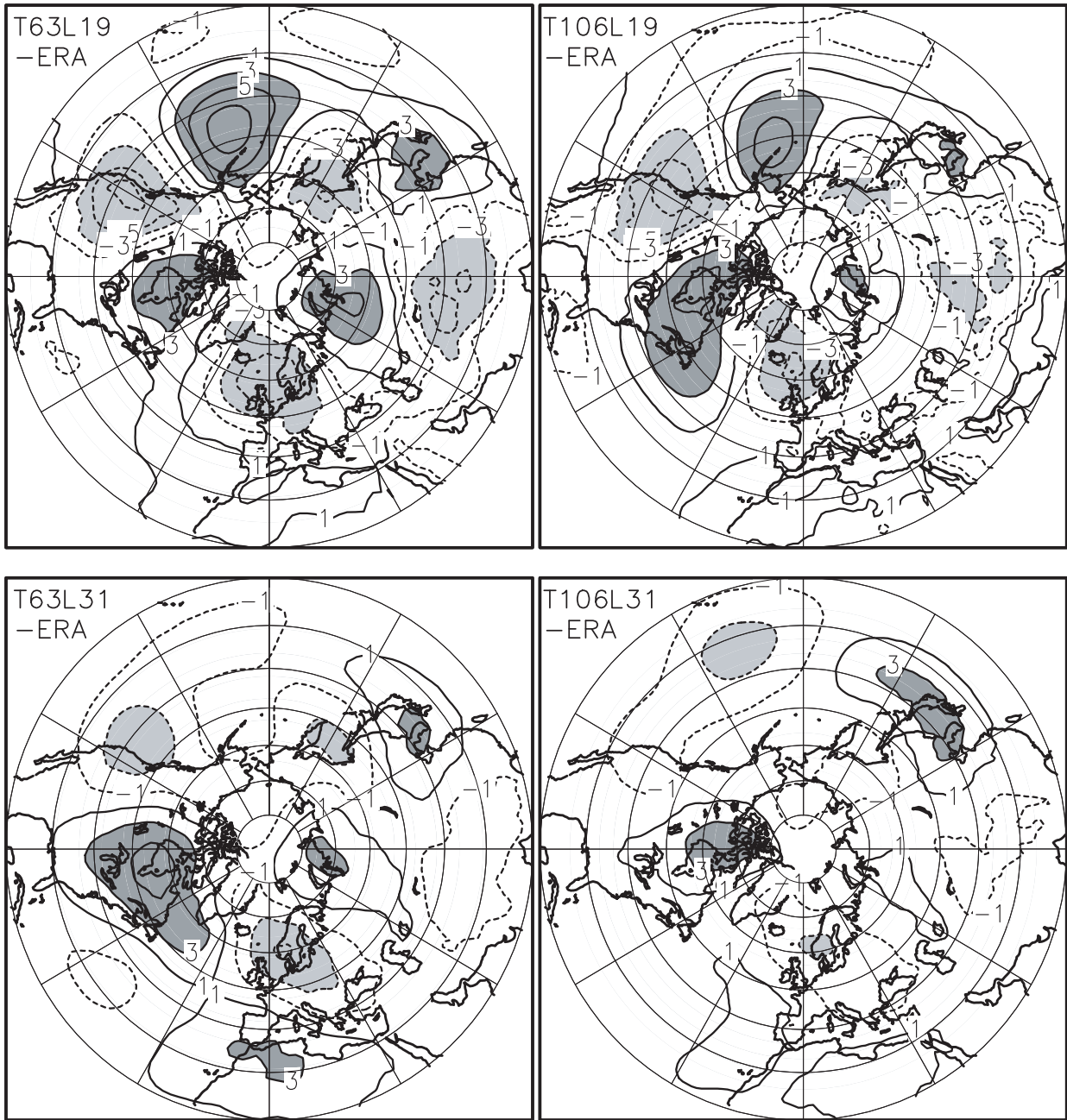


Figure 22: As Fig. 21 but for differences between model simulations and ERA-15. Contours are $\pm 1, 3, 5, 7$ decameter. Negative biases (< -3 decameter) are emphasized by light shading, positive biases (> 3 decameter) by dark shading.

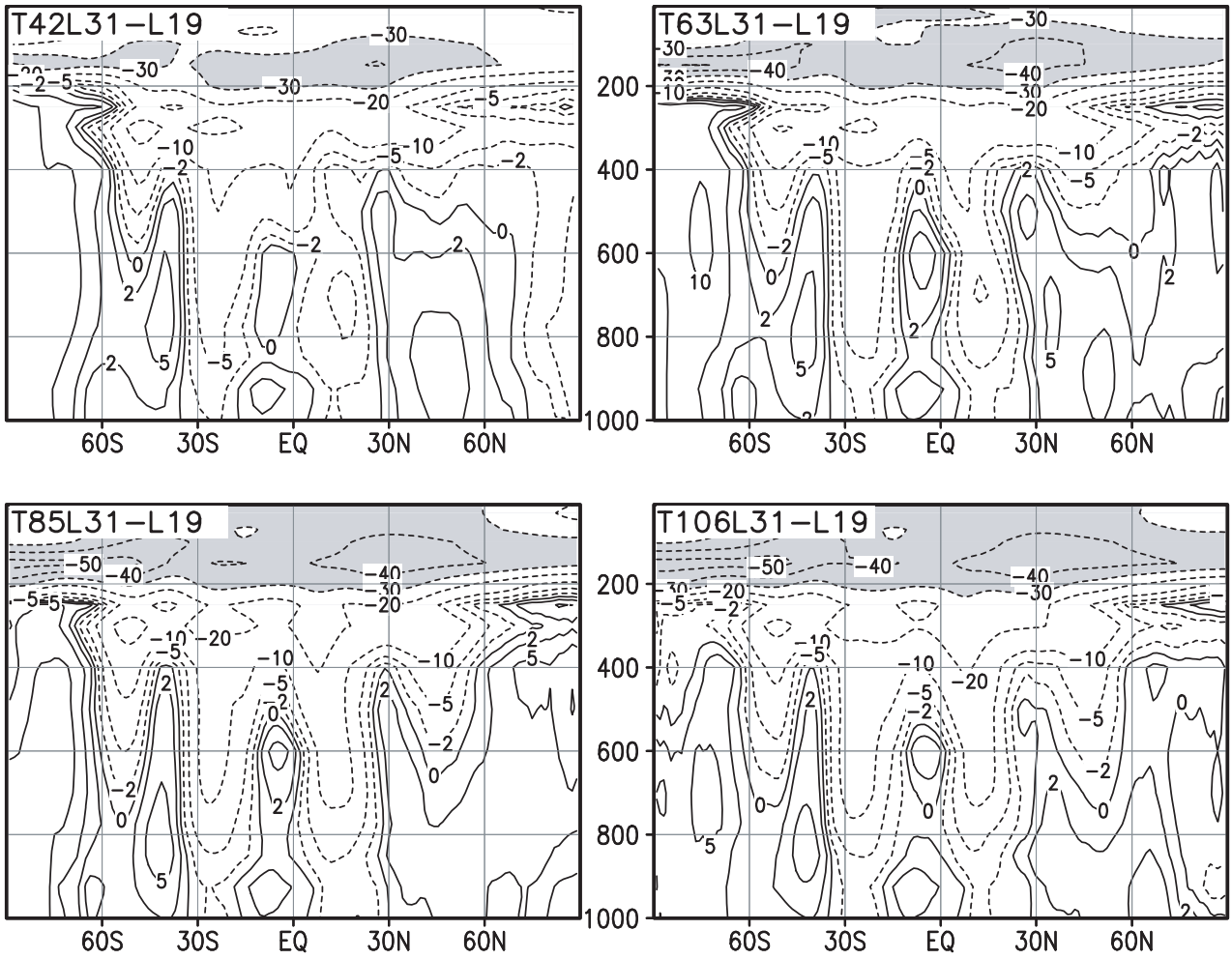


Figure 23: Relative differences in DJF zonal mean specific humidity between L31 and L19 simulations expressed in percent of the respective L19 values for different horizontal resolutions. Contours are - 50, - 40, - 30, - 20, - 10, - 5, 0, 5, 10 %. Light shading for differences < -30 %.

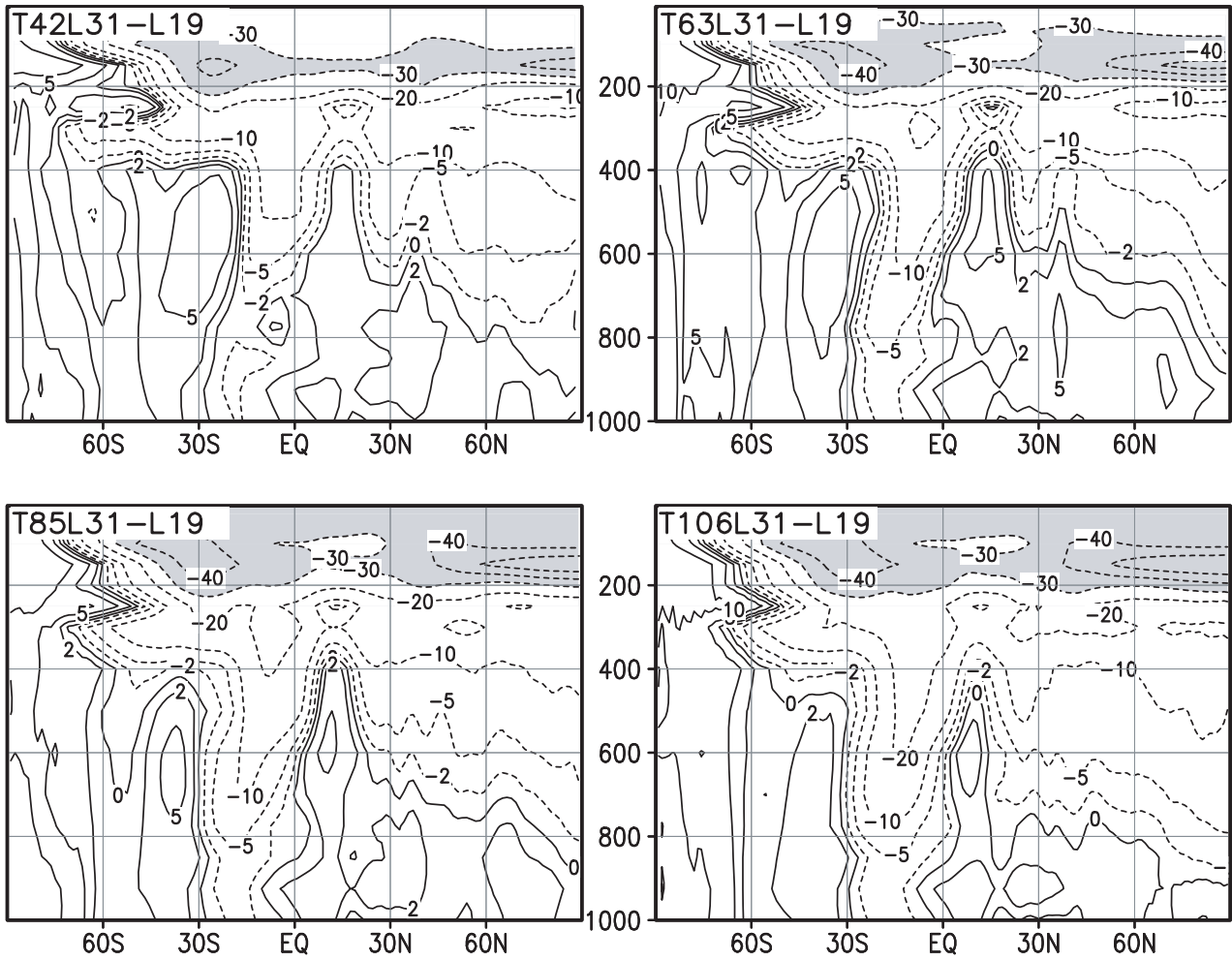


Figure 24: As Fig. 23 but for JJA.

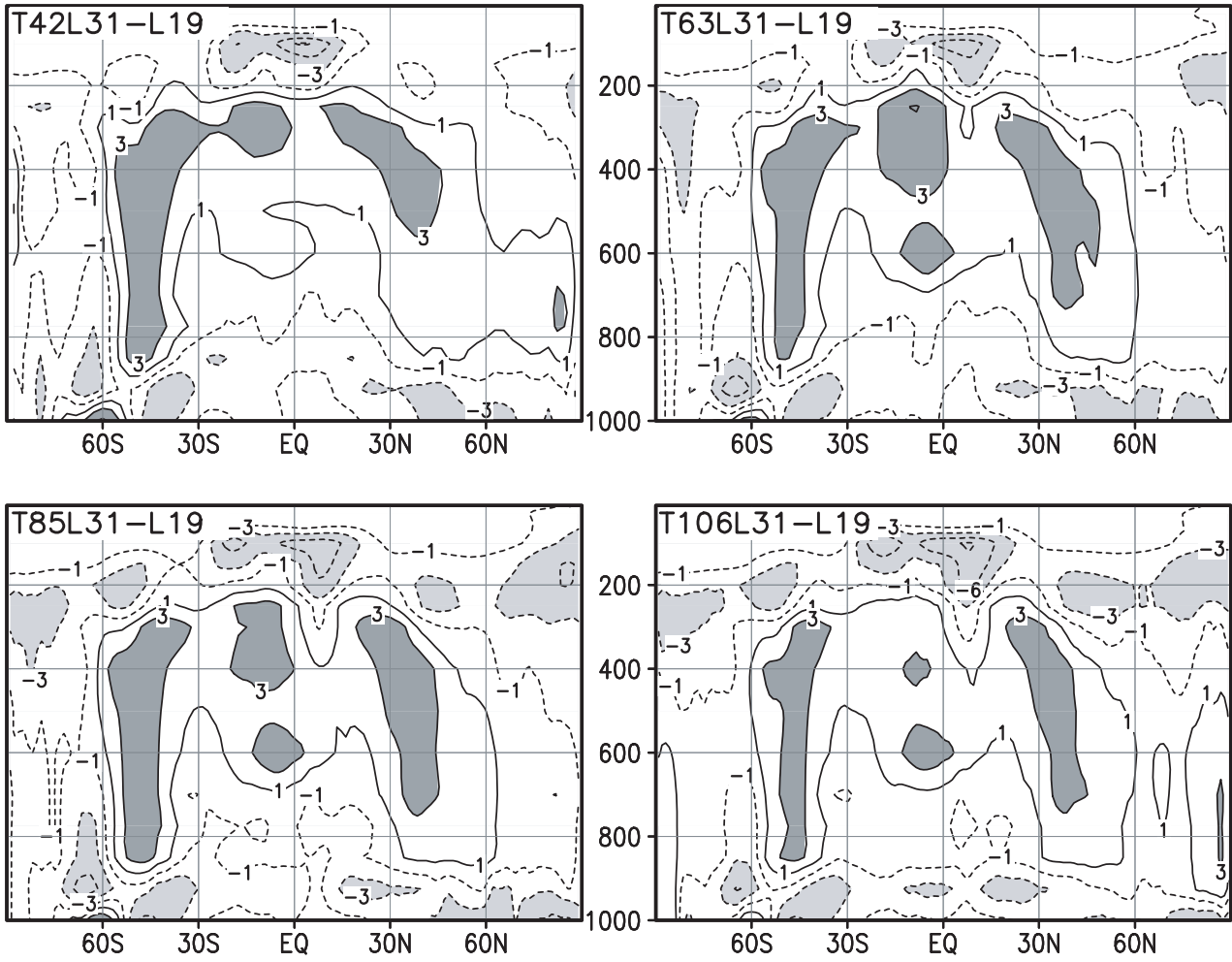


Figure 25: Differences in DJF zonal mean cloud cover between L31 and L19 simulations. Contours are $-9, -6, -3, -1, 1, 3, 6$ %. Light shading for differences < -3 %. Dark shading for differences > 3 %.

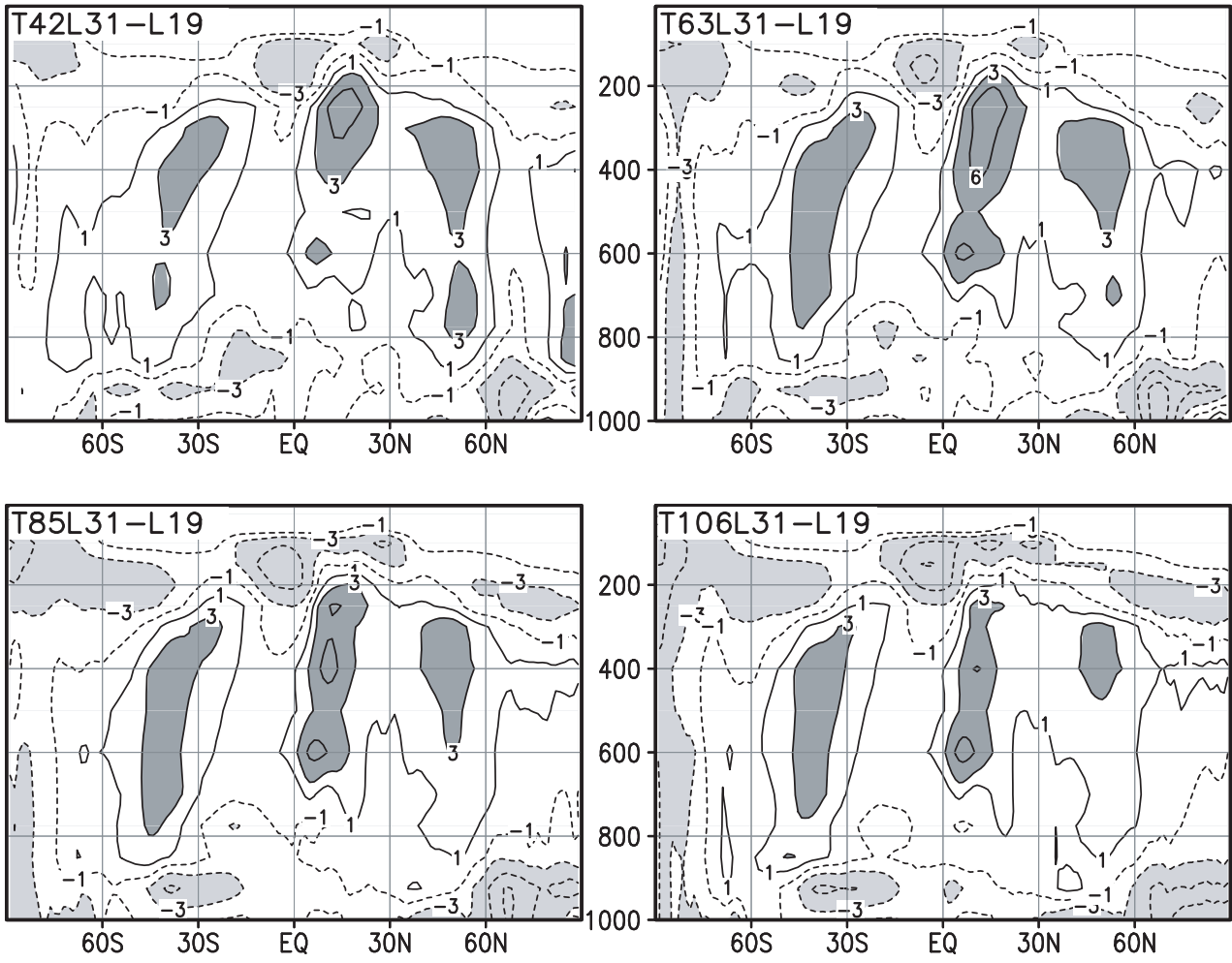


Figure 26: As Fig. 25 but for JJA.

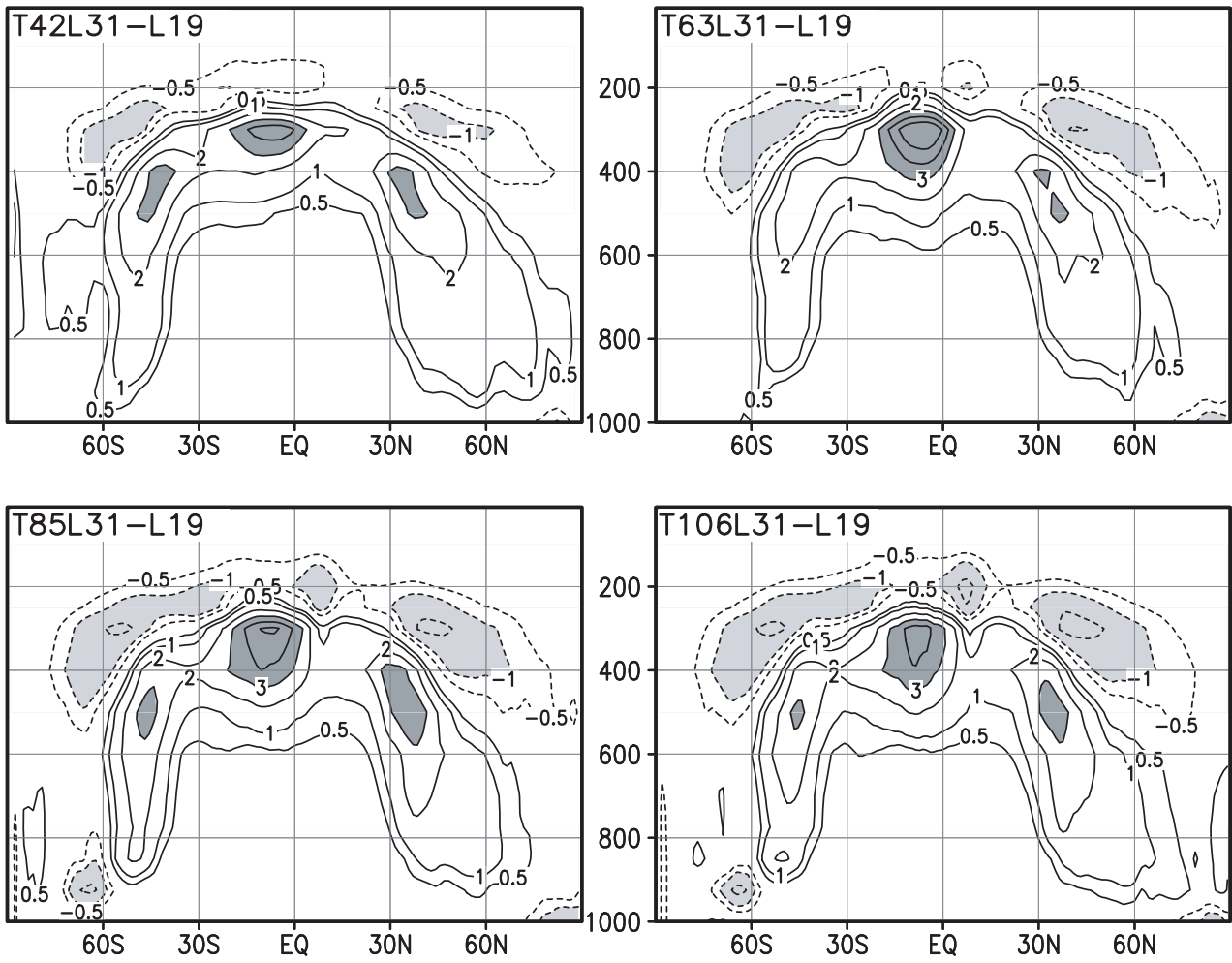


Figure 27: Differences in DJF zonal mean cloud ice mixing ratio. Contours are $\pm 0.5, 1, 2, 3, 4, 5$ mg/kg. Light shading for differences < -1 mg/kg. Dark shading for differences > 3 mg/kg.

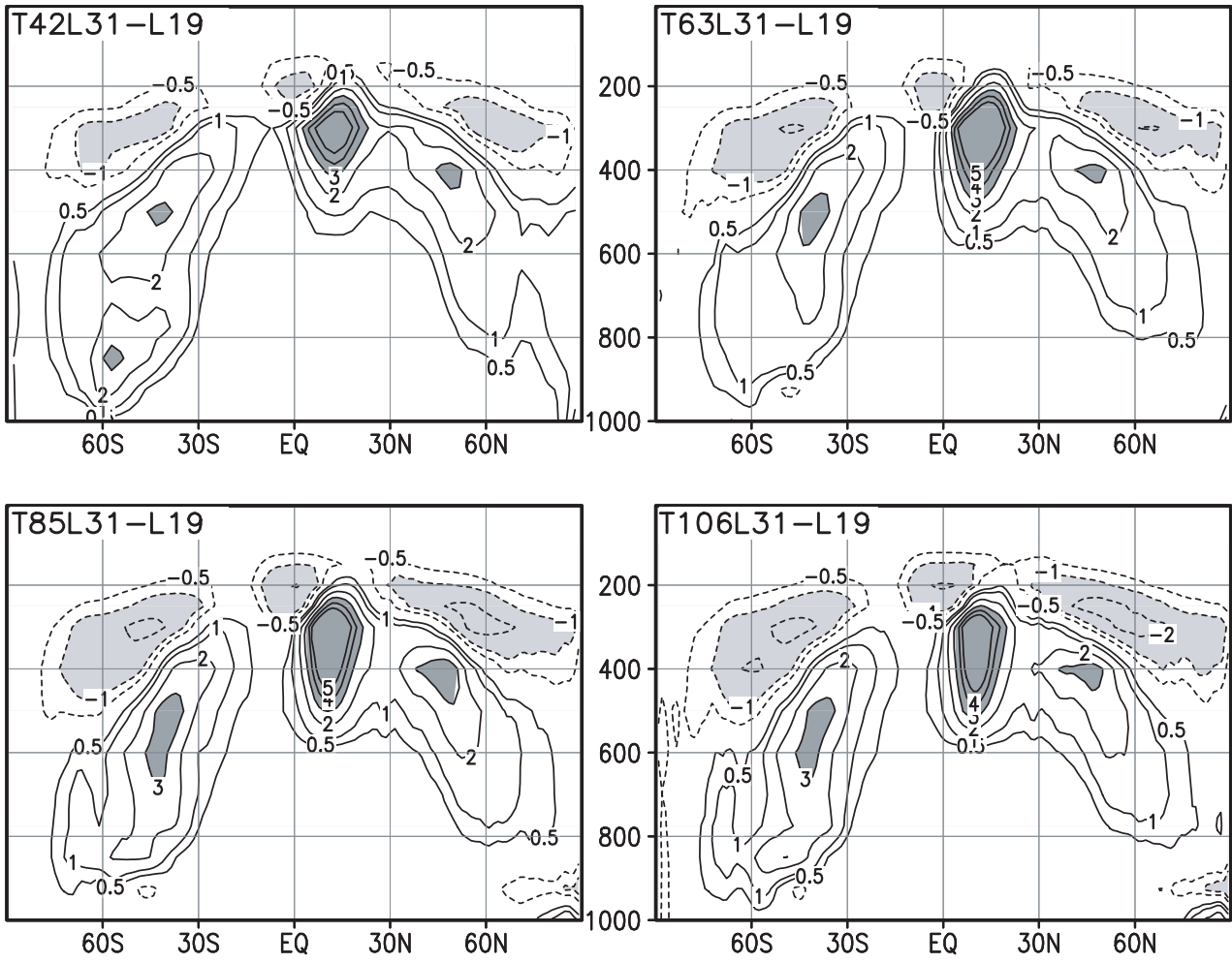


Figure 28: As Fig. 27 but for JJA.

- Report 1 - 302** Please order the reference list from MPI for Meteorology, Hamburg
- Report No. 303**
December 1999
The leading variability mode of the coupled troposphere-stratosphere winter circulation in different climate regimes
Judith Perlwitz, Hans-F. Graf, Reinhard Voss
* Journal of Geophysical Research, 105, 6915-6926, 2000
- Report No. 304**
January 2000
Generation of SST anomalies in the midlatitudes
Dietmar Dommenges, Mojib Latif
* Journal of Climate, 1999 (submitted)
- Report No. 305**
June 2000
Tropical Pacific/Atlantic Ocean Interactions at Multi-Decadal Time Scales
Mojib Latif
* Geophysical Research Letters, 28,3,539-542,2001
- Report No. 306**
June 2000
On the Interpretation of Climate Change in the Tropical Pacific
Mojib Latif
* Journal of Climate, 2000 (submitted)
- Report No. 307**
June 2000
Observed historical discharge data from major rivers for climate model validation
Lydia Dümenil Gates, Stefan Hagemann, Claudia Golz
- Report No. 308**
July 2000
Atmospheric Correction of Colour Images of Case I Waters - a Review of Case II Waters - a Review
D. Pozdnyakov, S. Bakan, H. Grassl
* Remote Sensing of Environment, 2000 (submitted)
- Report No. 309**
August 2000
A Cautionary Note on the Interpretation of EOFs
Dietmar Dommenges, Mojib Latif
* Journal of Climate, 2000 (submitted)
- Report No. 310**
September 2000
Midlatitude Forcing Mechanisms for Glacier Mass Balance Investigated Using General Circulation Models
Bernhard K. Reichert, Lennart Bengtsson, Johannes Oerlemans
* Journal of Climate, 2000 (accepted)
- Report No. 311**
October 2000
The impact of a downslope water-transport parameterization in a global ocean general circulation model
Stephanie Legutke, Ernst Maier-Reimer
- Report No. 312**
November 2000
The Hamburg Ocean-Atmosphere Parameters and Fluxes from Satellite Data (HOAPS): A Climatological Atlas of Satellite-Derived Air-Sea-Interaction Parameters over the Oceans
Hartmut Graßl, Volker Jost, Ramesh Kumar, Jörg Schulz, Peter Bauer, Peter Schlüssel
- Report No. 313**
December 2000
Secular trends in daily precipitation characteristics: greenhouse gas simulation with a coupled AOGCM
Vladimir Semenov, Lennart Bengtsson
- Report No. 314**
December 2000
Estimation of the error due to operator splitting for micro-physical-multiphase chemical systems in meso-scale air quality models
Frank Müller
* Atmospheric Environment, 2000 (submitted)
- Report No. 315**
January 2001
Sensitivity of global climate to the detrimental impact of smoke on rain clouds (only available as pdf-file on the web)
Hans-F. Graf, Daniel Rosenfeld, Frank J. Nober
- Report No. 316**
March 2001
Lake Parameterization for Climate Models
Ben-Jei Tsuang, Chia-Ying Tu, Klaus Arpe
- Report No. 318**
March 2001
On North Pacific Climate Variability
Mojib Latif
* Journal of Climate, 2001 (submitted)

- Report 1 - 302** Please order the reference list from MPI for Meteorology, Hamburg
- Report No. 319** **The Madden-Julian Oscillation in the ECHAM4 / OPYC3 CGCM**
 March 2001 Stefan Liess, Lennart Bengtsson, Klaus Arpe
 * Climate Dynamics, 2001 (submitted)
- Report No. 320** **Simulated Warm Polar Currents during the Middle Permian**
 May 2001 A. M. E. Winguth, C. Heinze, J. E. Kutzbach, E. Maier-Reimer,
 U. Mikolajewicz, D. Rowley, A. Rees, A. M. Ziegler
 * Paleoclimatology, 2001 (submitted)
- Report No. 321** **Impact of the Vertical Resolution on the Transport of Passive Tracers
 in the ECHAM4 Model**
 June 2001 Christine Land, Johann Feichter, Robert Sausen
 * Tellus, 2001 (submitted)
- Report No. 322** **Summer Session 2000
 Beyond Kyoto: Achieving Sustainable Development**
 August 2001 Edited by Hartmut Graßl and Jacques Léonardi
- Report No. 323** **An atlas of surface fluxes based on the ECMWF Re-Analysis-
 a climatological dataset to force global ocean general circulation
 models**
 July 2001 Frank Röske
- Report No. 324** **Long-range transport and multimedia partitioning of semivolatile
 organic compounds:
 A case study on two modern agrochemicals**
 August 2001 Gerhard Lammel, Johann Feichter, Adrian Leip
 * Journal of Geophysical Research-Atmospheres, 2001 (submitted)
- Report No. 325** **A High Resolution AGCM Study of the El Niño Impact on the North
 Atlantic / European Sector**
 August 2001 Ute Merkel, Mojib Latif
 * Geophysical Research Letters, 2001 (submitted)
- Report No. 326** **On dipole-like variability in the tropical Indian Ocean**
 August 2001 Astrid Baquero-Bernal, Mojib Latif
 * Journal of Climate, 2001 (submitted)
- Report No. 327** **Global ocean warming tied to anthropogenic forcing**
 August 2001 Bernhard K. Reichert, Reiner Schnur, Lennart Bengtsson
 * Geophysical Research Letters, 2001 (submitted)
- Report No. 328** **Natural Climate Variability as Indicated by Glaciers and Implications
 for Climate Change: A Modeling Study**
 August 2001 Bernhard K. Reichert, Lennart Bengtsson, Johannes Oerlemans
 * Journal of Climate, 2001 (submitted)
- Report No. 329** **Vegetation Feedback on Sahelian Rainfall Variability in a Coupled
 Climate Land-Vegetation Model**
 August 2001 K.-G. Schnitzler, W. Knorr, M. Latif, J. Bader, N. Zeng
 Geophysical Research Letters, 2001 (submitted)
- Report No. 330** **Structural Changes of Climate Variability (only available as pdf-file on the web)**
 August 2001 H.-F. Graf, J. M. Castanheira
 Journal of Geophysical Research -Atmospheres, 2001 (submitted)
- Report No. 331** **North Pacific - North Atlantic relationships under stratospheric
 control? (only available as pdf-file on the web)**
 August 2001 H.-F. Graf, J. M. Castanheira
 Journal of Geophysical Research -Atmospheres, 2001 (submitted)
- Report No. 332** **Using a Physical Reference Frame to study Global Circulation
 Variability (only available as pdf-file on the web)**
 September 2001 H.-F. Graf, J. M. Castanheira, C.C. DaCamara, A. Rocha

- Report 1 - 302** Please order the reference list from MPI for Meteorology, Hamburg

Journal of Atmospheric Sciences, 2001 (in press)
- Report No. 333** **Stratospheric Response to Global Warming in the Northern Hemisphere Winter**
November 2001
Zeng-Zhen Hu
- Report No. 334** **On the Role of European and Non-European Emission Sources for the Budgets of Trace Compounds over Europe**
October 2001
Martin G. Schultz, Johann Feichter, Stefan Bauer, Andreas Volz-Thomas
- Report No. 335** **Slowly Degradable Organics in the Atmospheric Environment and Air-Sea Exchange**
November 2001
Gerhard Lammel
- Report No. 336** **An Improved Land Surface Parameter Dataset for Global and Regional Climate Models**
January 2002
Stefan Hagemann
- Report No. 337** **Lidar intercomparisons on algorithm and system level in the frame of EARLINET**
May 2002
Volker Matthias, J. Bösenberg, H. Linné, V. Matthias, C. Böckmann, M. Wiegner, G. Pappalardo, A. Amodeo, V. Amiridis, D. Balis, C. Zerefos, A. Ansmann, I. Mattis, U. Wandinger, A. Boselli, X. Wang, A. Chaykovski, V. Shcherbakov, G. Chourdakis, A. Papayannis, A. Comeron, F. Rocadenbosch, A. Delaval, J. Pelon, L. Sauvage, F. DeTomasi, R. M. Perrone, R. Eixmann, J. Schneider, M. Frioud, R. Matthey, A. Hagard, R. Persson, M. Iarlori, V. Rizi, L. Konguem, S. Kreipl, G. Larchevêque, V. Simeonov, J. A. Rodriguez, D. P. Resendes, R. Schumacher
- Report No. 338** **Intercomparison of water and energy budgets simulated by regional climate models applied over Europe**
June 2002
Stefan Hagemann, Bennert Machenhauer, Ole Bøssing Christensen, Michel Déqué, Daniela Jacob, Richard Jones, Pier Luigi Vidale
* Climate Dynamics (submitted)
- Report No. 339** **Modelling the wintertime response to upper tropospheric and lower stratospheric ozone anomalies over the North Atlantic and Europe**
September 2002
Ingo Kirchner, Dieter Peters
- Report No. 340** **On the determination of atmospheric water vapour from GPS measurements**
November 2002
Stefan Hagemann, Lennart Bengtsson, Gerd Gendt
* J. Geophys. Res., 2003, Vol. 108, No. D21, 4678
- Report No. 341** **The impact of international climate policy on Indonesia**
November 2002
Armi Susandi, Richard S.J. Tol
- Report No. 342** **Indonesian smoke aerosols from peat fires and the contribution from volcanic sulfur emissions** (only available as pdf-file on the web)
December 2002
Bärbel Langmann, Hans F. Graf
- Report No. 343** **Modes of the wintertime Arctic temperature variability**
January 2003
Vladimir A. Semenov, Lennart Bengtsson
- Report No. 344** **Indicators for persistence and long-range transport potential as derived from multicompartment chemistry-transport modelling**
February 2003
Adrian Leip, Gerhard Lammel
- Report No. 345** **The early century warming in the Arctic – A possible mechanism**
February 2003
Lennart Bengtsson, Vladimir A. Semenov, Ola Johannessen
- Report No. 346** **Variability of Indonesian Rainfall and the Influence of ENSO and Resolution in ECHAM4 Simulations and in the Reanalyses**
May 2003
Edvin Aldrian, Lydia Dümenil Gates, F. Heru Widodo

Report 1 - 302

Please order the reference list from MPI for Meteorology, Hamburg

Report No. 347
June 2003

Sensitivity of Large Scale Atmospheric Analyses to Humidity Observations and its Impact on the Global Water Cycle and Tropical and Extra-Tropical Weather Systems
L. Bengtsson, K. I. Hodges, S. Hagemann
* Tellus (accepted)

Report No. 348
September 2003

EARLINET: A European Aerosol Research Lidar Network to Establish an Aerosol Climatology
J. Bösenberg, V. Matthias, et al.

Report No. 349
November 2003

The atmospheric general circulation model ECHAM 5. PART I: Model description
E. Roeckner, G. Bäuml, L. Bonaventura, R. Brokopf, M. Esch, M. Giorgetta, S. Hagemann, I. Kirchner, L. Kornbluh, E. Manzini, A. Rhodin, U. Schlese, U. Schulzweida, A. Tompkins

Report No. 350
December 2003

Principles of variational assimilation of GNSS radio occultation data
M. E. Gorbunov, L. Kornbluh

Report No. 351
January 2004

Can Climate Trends be Calculated from Re-Analysis Data?
L. Bengtsson, S. Hagemann, K. I. Hodges

Report No. 352
January 2004

Tropical Pacific Decadal Variability and the Subtropical-Tropical Cells
K. Lohmann, M. Latif

Report No. 353
Juli 2004

CO₂-Reduktion und Energieeffizienz im Straßengüterverkehr
Jacques Léonardi, Michael Baumgartner, Oliver Krusch

ISSN 0937 - 1060